2016-06-01

In Situ Magnetic Field Characterization with the Directional Hanle Effect

Jarom Silver Jackson
Brigham Young University

BYU ScholarsArchive Citation

Jackson, Jarom Silver, "In Situ Magnetic Field Characterization with the Directional Hanle Effect" (2016). *All Theses and Dissertations*. 5982.
https://scholarsarchive.byu.edu/etd/5982

In Situ Magnetic Field Characterization with the

Directional Hanle Effect

Jarom Silver Jackson

A thesis submitted to the faculty of
Brigham Young University
in partial fulfillment of the requirements for the degree of

Master of Science

Dallin S. Durfee, Chair
Jean-Francois S. Van Huele
Michael J. Ware

Department of Physics and Astronomy

Brigham Young University

June 2016

ABSTRACT

In Situ Magnetic Field Characterization with the Directional Hanle Effect

Jarom Silver Jackson
Department of Physics and Astronomy, BYU
Master of Science

We present a novel method of in situ magnetic field mapping related to the Hanle effect. This method uses the change in spatial radiation pattern of scattered light, which we call a ‘directional Hanle effect,’ rather than the loss of polarization more commonly associated with the Hanle effect. It is particularly well suited for fields in a magneto-optical trap (MOT), requiring only the addition of a narrow slit and a camera to typical MOT components. The use of this method is demonstrated by measuring the gradient through, and location of, the zero-point of the field in our strontium MOT.

Keywords: Hanle effect, laser cooling, magnetic field, magnetic tomography, magneto-optical trap

ACKNOWLEDGMENTS

I’d like to acknowledge the support of everybody who has made my pursuit of this research possible, including my family, my advisor, and the BYU physics department. Most of all, I am grateful for the support of my wife, who has supported me and kept me motivated when I was down, frustrated, or considering abandoning my pursuit of a masters degree.

Contents

Chapter 1

Introduction

1.1 Magnetic field measurement

Magnetic fields are frequently used in a vacuum for experiments involving laser cooling (as well as many other areas of science). Characteristics of these fields, such as locations where the field goes to zero and the field gradient and curvature through such points must meet requirements specified by the nature of the experiment. The field must be designed carefully to satisfy these requirements. In many cases careful design, and testing of the field generator (e.g. current loops, or permanent magnets) separate from the vacuum system is sufficient. In some cases, however, it may be necessary to measure characteristics of a field in situ in the vacuum environment. This can be a difficult task in practice. This thesis introduces a method to characterize magnetic fields using resonances in an atomic vapor. It is particularly suited for, and simple to use in, atomic physics experiments dealing with magneto optical traps (MOTs) or other similar experimental setups.

Various methods for characterizing or full 3D mapping of fields have been demonstrated previously. The most simple and direct method is to use a physical probe, such as a Hall effect sensor to probe each point in space. The physical size of a Hall probe can be an obstacle, as well as calibration drift. If the region of interest is inside a vacuum it can be difficult to gain physical access without contaminating the vacuum environment. Experiments involving laser cooling and trapping generally have this limitation. Due to the nature of such experiments, however, there are often other ways of measuring fields.

Atomic physics experiments often have lasers designed to probe atoms, which are sensitive to magnetic fields, in the vacuum. This opens up the possibility for various in situ magnetic field measurement techniques. Methods described in the literature for this type of field measurement include use of the Hanle effect [1,2], the mechanical Hanle effect [3], and various methods of spectroscopic fluorescence imaging [4,5]. These methods are not generally applicable in all situations. They may require additional (and expensive) equipment, a particular vacuum chamber design, or a significant amount of additional engineering.

The purpose of this thesis is to detail a method of field mapping we have developed that should be applicable in any MOT based experiment. We demonstrate the use of this method to find the location of the zero-point in the magnetic field, which is important for MOT alignment. We also measure the field gradient through the zero-point, which determines the size and trapping rate of the MOT. The method is easy to implement (if applicable) and requires little additional equipment or setup. As with some methods mentioned above [1–3], this method is related to the Hanle effect, though it uses directionality of radiation rather than polarization, is more broadly applicable, and is easier to implement.

1.2 Intro to the Hanle effect

The spontaneous emission from atoms stimulated by resonant, linearly polarized light is typically polarized in the same direction as the stimulating light. The Hanle effect refers to the reduction in the degree of polarization of such light due to the presence of a magnetic field.

The Hanle effect was named after Wilhelm Hanle, who gave the first physically accurate description of the effect in 1924 [6]. It had been discovered that the polarization of resonant fluorescence from stimulated mercury atoms changed in the presence of a magnetic field. Hanle was able to explain this by viewing the fluorescence as emanating from a dipole with an exponentially decaying oscillation that rotates in a magnetic field.

The Hanle effect has been used in a variety of spectroscopic experiments. In such experiments it is generally used with a controlled magnetic field to measure transition lifetimes. We reverse these roles, and use a known lifetime, and fluorescence from the atom to measure an unknown field. The Hanle effect has been use in this way to measure magnetic fields in astronomy [7], and in a limited way in at least one atomic physics experiment (though only to establish an upper limit) [1]. In contrast, our method in principle allows full mapping of a field in a vacuum. Additionally, unlike other experiments involving the Hanle effect, our method depends on how a magnetic field changes the direction of outgoing radiation, rather than the polarization or changes in atomic trajectories.

1.3 Intro to the directional Hanle effect

The key to our field characterization method is that a magnetic field shifts not only the polarization of scattered light, but the outgoing radiation pattern as well. The change in radiation pattern affects the intensity of scattered light reaching an observer, so a simple intensity measurement is sufficient.

The relationship between the polarization and directionality of scattered light can be seen with a semi-classical treatment of resonant scattering by treating the atom as a damped oscillating dipole. In the absence of a magnetic field, atoms that are excited by linearly polarized light give off linearly polarized light, and are modeled as an oscillating dipole with the axis parallel to the polarization of the exciting light. The presence of a magnetic field causes the oscillating dipole to rotate, changing both the polarization and the directionality of light.

A classical linearly oscillating dipole emits no light on axis. It has radiation pattern proportional to $\sin^2\theta$, where θ is the angle of the observer from the dipole axis. A magnetic field causes the dipole to rotate, however, so that there is some light emitted along the original axis. We can take advantage of this by stimulating atoms with a linearly polarized laser, then viewing fluorescence given off in the direction of polarization. Only atoms in a magnetic field will give off radiation in this direction, so an observer will ‘see’ zero-points in the magnetic field, since they show up as dark spots in the fluorescence.

For our experiment we are primarily interested in finding the location of a field zero-point and the gradient through that point (though in principle we could use our method to measure the exact shape of the field in low magnetic field regions). We do so by sending polarized light through a slit to illuminate a thin slice within a vacuum vapor cell, then viewing the region from a direction perpendicular to the beam and the slit, but parallel to the polarization. The location of zero-points in the field are given by the dark spots, and the gradient through those points can be determined by the width of the spots.

This method should be readily applicable if the field gradient is in the range such that $L_\mathrm{p} < \mathrm{D} \lesssim L_\mathrm{i}$ where L_p is the smallest detectable feature (i.e. effective pixel size), D is the width of the observed dark spot, and L_i is the size of the imageable region. The MOT trapping radius (and therefore the optimal beam width) is also approximately equal to D, such that the above condition is true in general for MOT experiments with properly tuned beam widths and field gradients. This makes these dark spots a very intuitive and simple measurement of the trapping region in any MOT experiment.

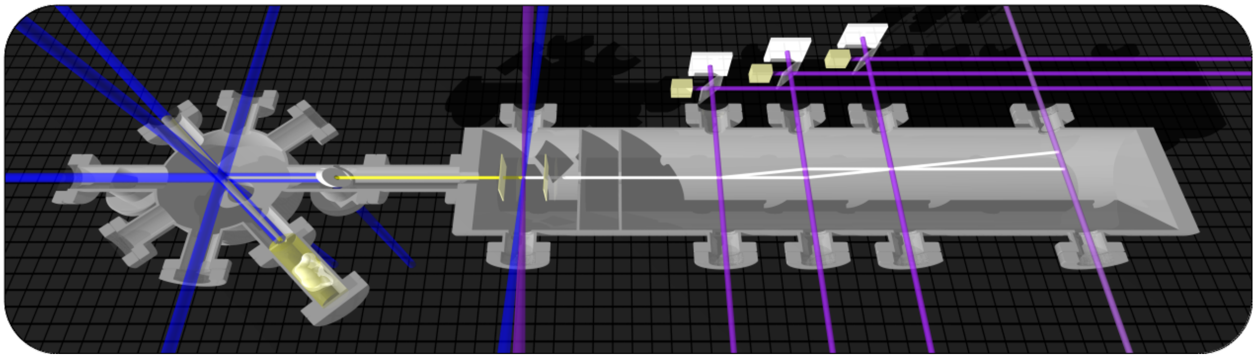

Figure 1.1 Drawing of a proposed ion interferometer using photoionized laser cooled Sr from a MOT, and a series of optical Raman diffraction gratings.

1.4 Experimental context

The long term goal of our research is to build a first of it's kind cold ion interferometer, and use it to perform precision tests of electromagnetic theory and other experiments. We are using strontium because it is readily cooled and, once ionized, has a level structure we can use to make optical gratings and generate matterwave interference effects. The vacuum chambers and lasers needed for this are depicted in Fig. 1.1.

There are various significant challenges in achieving cold, controlled and measurable matterwave interference. The first step for us is to cool the neutral strontium using a magneto optical trap. This trap will have a small hole in the trapping potential through which atoms will leak once they have been adequately cooled. After escaping the trap this stream of atoms will be accelerated into the interference chamber where they will be ionized using a two photon transition to an autoionizing state in the continuum. After they are ionized the atoms will pass through a series of $\pi/2$ and π pulses which will split their wave functions along two paths, and then recombine them. A probe laser at the end will read off the state so we can analyze the interference effects.

We are currently working on generating a steady controllable stream of atoms from the MOT. Difficulties with getting the experimental parameters right led us to search for a way to characterize the magnetic field, and properly align the magnets and beams. This inspired the development of the Hanle effect related measurement that is the focus of this thesis. Understanding the context of the development of this method will hopefully help in understanding the usefulness of the method, and the way in which it was developed.

All of the experimental work and data presented herein were only possible thanks to the work that had previously been done towards making the ion interferometer. The ground work was mostly done by Chris Erickson [8]. The vacuum chambers, optical layouts and electronics setup were done prior to the start of my project. A MOT had been successfully formed, albeit in unstable conditions that prevented further progress. Unfortunately, much of this work had to be redone due to lab mishaps and lessons learned the first time through.

We began working on the laser cooling setup after a vacuum window had imploded, requiring the vacuum chamber and most of the cooling optics to be removed. At about the same time we had decided to replace the cooling laser used previously due to it's instability. As such we had to rebuild much of the trapping experiment, including baking out the vacuum, replacing windows, redoing the optical layout, working with a new laser and learning how to work with strontium vapor.

Much of this work was facilitated by the work and the design done previously but there were some significant hurdles as well. We were not able to achieve cooling initially, even after attempting to redo Erickson's work, because of a few unfortunate differences in our new setup. The main issues were increased reflectivity of the new windows, significantly less power available from the new laser (about half) and heat damage done to the permanent magnets causing a shift in the magnetic field zero-points.

After failing to trap atoms with the same setup used previously, we realized our tolerances were much tighter. Less optical power meant we needed the beams to be smaller. The smaller beams and shifted field zeros made it impossible to trap atoms without some way to align them all beyond the rough mechanical alignment that had worked before. This is what motivated my research into the directional Hanle effect. The alignment procedure is described in Appendix B.

Chapter 2

Hanle Effect Theory

This chapter will introduce the theory behind the Hanle effect, and the ‘directional’ Hanle effect. In our approach we will treat atoms as individual oscillating dipoles. The first step (see Sec. 2.1) is to understand radiation from a classical oscillating dipole. The following section will discuss light-atom interactions and the connection between classical values (such as the dipole strength and radiated power), and constants of the atom transition (such as the transition lifetime and the matrix element of the dipole operator between the two states of the transition). Understanding these principles will help in understanding the derivation of the Hanle effect (Sec. 2.4), and the directional Hanle effect (Sec. 2.5) later in this chapter.

In deriving the Hanle effect we will make the assumption that the rate of stimulation and spontaneous emission is equal for all transitions in an atom, and across all atoms in the ensemble. In practice, this assumption is true for broadband stimulating light, but not for a narrow wavelength source such as the laser used in our experiments. Though the assumption is not completely accurate, it does allow us to get some useful analytical results. A more complete analysis including rate dependence is discussed in Sec. 2.6.

2.1 Dipole radiation patterns

We will start by examining the outgoing radiation from a classical oscillating electric dipole. This is a reasonable model for resonant spontaneous emission from atoms stimulated by a laser if the number of atoms and photons is large enough, and interactions between the atoms and scattered light can be ignored (which is this case if the density of atoms is low enough that the intensity of the scattered light is much less than that of the stimulating light) [9, pg. 355]. Such a dipole can be written as $\mathbf{d}\cos(\omega t)$ where the amplitude d, and frequency ω are properties of the atomic transition and the driving light (see Sec. 2.2). We will follow the convention of treating time dependence with complex exponentials ($\exp(i\omega t)$), with the real part understood to give the actual field and dipole values.

A classical linear oscillating dipole (e.g. with all real components) emits radiation in all directions except along its axis. We are interested in direction and polarization of the radiation, as well as the total power radiated. Calculating the general expression for this radiation in the far field is a common textbook problem. The result, as a coordinate-free expression, is

$$\begin{aligned}\mathbf{E}(\mathbf{r}) &= \frac{k^2}{4\pi\varepsilon_0}(\hat{\mathbf{r}}\times\mathbf{d})\times\hat{\mathbf{r}}\frac{e^{ikr-i\omega t}}{r} \\ &= \frac{k^2}{4\pi\varepsilon_0}(\hat{\mathbf{r}}\times\mathbf{d})\times\hat{\mathbf{r}}\frac{e^{-i\omega t_r}}{r},\end{aligned} \tag{2.1}$$

where $k = \omega/c$, ε_0 is the electric vacuum permittivity, and c is the speed of light. This is further simplified in the second line by substituting a 'retarded time' $t_r = t - r/c$, for t. The retarded time represents the time at which dipole mechanics occurred that caused the field at the observation point at the lab time t. For all intents and purposes, we care more about what is going on at the dipole itself, so we'll continue to use t_r as our time variable, and keep in mind that what we are actually observing and calculating is the field that results far from the dipole, i.e. the radiation field.

The result above can be extended to include circular or elliptical oscillations by treating them as the sum of two perpendicular linear dipoles with a phase offset. For example, a dipole along $\hat{\mathbf{x}}$ added to a dipole of equal magnitude along $\hat{\mathbf{y}}$ oscillating at the same frequency, but 90° out of phase, forms a dipole rotating around the $\hat{\mathbf{z}}$ axis. By allowing d to be the sum of two complex vectors in different directions, the phase offset is encoded in the angle between the two vectors in the complex plane. A useful way to keep track of left and right circular dipole rotations is to define a new set of basis vectors for dipole and light polarization, where $\hat{\mathbf{e}}_1$ represents orientation with the z axis, and $\hat{\mathbf{e}}_\pm$ represent right or left polarizations. In terms of the Cartesian unit vectors, these are:

$$\begin{aligned} \hat{\mathbf{e}}_1 &= \hat{\mathbf{z}} \\ \hat{\mathbf{e}}_+ &= \frac{1}{\sqrt{2}}(\hat{\mathbf{x}} + i\hat{\mathbf{y}}) \\ \hat{\mathbf{e}}_- &= \frac{1}{\sqrt{2}}(\hat{\mathbf{x}} - i\hat{\mathbf{y}}). \end{aligned} \tag{2.2}$$

The expression $(\hat{\mathbf{r}} \times \mathbf{d}) \times \hat{\mathbf{r}}$ in Eq. (2.1) gives rise to various radiation patterns depending on the form of $\mathbf{d}$. This factor turns out to be where all directivity and polarization effects that we care about come from. As such, we will proceed to calculate this term for our $\hat{\mathbf{e}}_{1,\pm}$ basis vectors. We will give the results in terms of the spherical coordinate system (r, θ, ϕ) corresponding to our original coordinates, where θ and ϕ are the zenith and azimuthal angles, respectively. This gives

$$\begin{aligned} (\hat{\mathbf{r}} \times \hat{\mathbf{e}}_1) \times \hat{\mathbf{r}} &= -\sin\theta\,\hat{\theta} \\ (\hat{\mathbf{r}} \times \hat{\mathbf{e}}_\pm) \times \hat{\mathbf{r}} &= \frac{1}{\sqrt{2}}[(\cos\phi \pm i\sin\phi)\cos\theta\,\hat{\theta} - (\sin\phi \mp i\cos\phi)\hat{\phi}]. \end{aligned} \tag{2.3}$$

The intensity per solid angle is a constant $(\varepsilon_0(k^2/4\pi\varepsilon_0)^2)$ times the magnitude of the above vectors. Taking the magnitude gives

$$\begin{aligned} \|(\hat{\mathbf{r}} \times \hat{\mathbf{e}}_1) \times \hat{\mathbf{r}}\| &= \sin^2\theta \\ \|(\hat{\mathbf{r}} \times \hat{\mathbf{e}}_\pm) \times \hat{\mathbf{r}}\| &= \frac{1}{2}(\cos^2\theta + 1). \end{aligned} \tag{2.4}$$

To find the total power radiated, we integrate over all angles, and multiply by the constants out front. It turns out we get the same[1] answer for each of these oscillation states,

$$P_{\text{rad}} = \frac{cd^2k^4}{12\pi\varepsilon_0}. \tag{2.5}$$

2.2 Light atom interactions

A quantum description of the Hanle effect deals with quantization of energy levels in an atom, as well as photon interactions within the atom. A full treatment would require quantum electrodynamics. In our case, however, it is sufficient to give the atom a basic quantum description while maintaining a classical field description for the radiation fields [10, p. 13]. The goal of this section is to find the link between the classical model and the quantum model of the transition. This is through the transition dipole moment (or quadrupole, etc. for higher order forbidden transitions). In a two state atom this is the matrix element of the dipole operator for the two states, which is related to the classical dipole discussed above. We will show how the equivalent classical dipole strength is related to the quantum dipole operator. We will also summarize the physics important in determining the rate of emission as a function of detuning between the stimulating light and the transition.

For our purposes, the most important result is the directional dependence of radiation. The results from the previous section for a classical dipole are sufficient for this purpose. In this section we will discuss the connection between the classical dipole moment and the quantum dipole oper-

---

[1] There can be some confusion over a factor of two here. To clarify this, consider two dipoles of equal magnitude, and vary one sinusoidally in magnitude, and the other by spinning it at the same frequency. The rotating dipole will emit twice the power as the linearly oscillating dipole. In the complex representation the rotating dipole is the sum of two perpendicular linear dipoles of the original dipole's magnitude, resulting in a factor $\sqrt{2}$ difference in dipole magnitude, and a factor of 2 difference in power. Throughout this text, dipole magnitude will always refer to the complex modulus—not the magnitude of the corresponding stationary dipole (i.e. the amplitude of the real part of the dipole).

ator, and relate the magnitude of the classical radiation derived above, proportional to the dipole moment amplitude d, to the matrix element of the quantum dipole operator μ_{21}. We will also explain the exponential decay of the dipole moment that is important when deriving the Hanle effect, and discuss the dependence of the rate of spontaneous radiation on the frequency detuning of the probe laser.

We will summarize here the relations we need from a quantum description of light atom interactions. The following results and derivations are appropriate for a single atom interacting with an external field, such as a laser. These results are approximately accurate for an ensemble of atoms so long as the atoms do not significantly alter the radiation field [9, pg. 355]. We will derive the outgoing radiation I_r as a function of the stimulating laser intensity I_l (and other variables), which will be valid so long as $I_r \ll I_l$.

The atomic transition parameters of interest are the natural linewidth Γ (often called the Einstein coefficient, A_{21}), the frequency ω_0, and matrix element μ_{21} of the electric dipole operator $\boldsymbol{\mu}$ (μ is used here to avoid confusion with the classical dipole $\mathbf{d}$). The dipole moment is related [11] to Γ as

$$\mu_{21}^2 = \frac{3\varepsilon_0 h c^3}{2\omega_0^3}\Gamma,$$

where ε_0 is the constant of electric vacuum permittivity, and h is Plank's constant (see Appendix A).

To model spontaneous emission, we treat each atom as if it is an oscillating dipole of magnitude $d \propto \mu_{21}$. In an ensemble of atoms, we sum those excited at the same time and with the same initial phase. Each atom of this subset has a probability of decaying Γdt in an infinitesimal slice of time dt, such that the population of atoms remaining in the excited state, as well as the net intensity of the emitted light, after a time t of being in the excited state is proportional to $\exp(-\Gamma t)$. If the atoms are treated as a classical dipole, then we must include this exponential decay. Because of the square relationship between the intensity of radiation and the magnitude of an oscillating electric dipole, the dipole decays at a rate of $\gamma = \Gamma/2$ [10].

The electric field parameters, set by the stimulating laser, are

$$\begin{aligned}
&\lambda && \text{the laser wavelength,} \\
&I_l && \text{the measured laser intensity,} \\
&\hat{\mathbf{n}} && \text{propagation direction of the laser,} \\
&\hat{\mathbf{p}} && \text{the laser polarization,} \\
&\omega_l = 2\pi c/\lambda && \text{the laser frequency,} \\
&\delta_l = \omega_l - \omega_0 && \text{the laser detuning,} \\
&E_0 = \sqrt{2I_l/c\varepsilon_0} && \text{the electric field strength,} \\
&\mathbf{k} = (2\pi/\lambda)\hat{\mathbf{n}} && \text{the wave vector.}
\end{aligned} \tag{2.6}$$

These are summed up in the plane wave model for the stimulating electric field:

$$\mathbf{E} = E_0 e^{i\mathbf{k}\cdot\mathbf{r} - i\omega_l t}\hat{\mathbf{p}}. \tag{2.7}$$

We are now interested in the rate of spontaneous emission, and the total power of the spontaneous radiation from the atom. The spontaneous emission rate effectively allows us to relate the induced dipole strength μ_{21} to the field strength I_l. We will give this in terms of the saturation parameter s, which represents the saturation of the transition and is defined as

$$\begin{aligned}
s &= \frac{1}{c\varepsilon_0\hbar^2}\frac{\mu_{21}^2 I_l}{\delta_l^2 + (\Gamma^2/4)} \\
&= \frac{I_l}{I_s}\frac{1}{1 + 4(\delta_l/\Gamma)^2},
\end{aligned} \tag{2.8}$$

where we've defined a saturation intensity,

$$I_s = \frac{c\varepsilon_0\hbar^2\Gamma^2}{4\mu_{21}^2} = \frac{\hbar\omega_0^3\Gamma}{12\pi c^2}.$$

In terms of s and Γ, the time averaged rate of spontaneous emission is

$$\begin{aligned} R = \left\langle \frac{dN}{dt} \right\rangle &= \frac{1}{2}\frac{\Gamma s}{1+s} \\ &= \frac{\Gamma}{2}\frac{I}{I_s}\frac{1}{1+I/I_s+4\delta_l^2/\Gamma^2}, \end{aligned} \tag{2.9}$$

from which we obtain the total power emitted as

$$P = \hbar\omega\frac{\Gamma}{2}\frac{I}{I_s}\frac{1}{1+I/I_s+4\delta_l^2/\Gamma^2}. \tag{2.10}$$

Comparing Eq. (2.10) with Eq. (2.5), we can obtain a relation between the classical dipole moment **d** used in the Sec. 2.1 and the quantum dipole matrix element μ_{21}, which we do so to obtain

$$d^2 = \frac{6\pi\varepsilon_0\hbar\Gamma}{k^3}\frac{I}{I_s}\frac{1}{1+I/I_s+4\delta_l^2/\Gamma^2}. \tag{2.11}$$

For $s \ll 1$, this is linear with respect to intensity, but for $s \gg 1$, it approaches the constant value

$$d^2 = \frac{6\pi\varepsilon_0\hbar\Gamma}{k^3}. \tag{2.12}$$

2.3 Zeeman shift

The effect that magnetic fields have on atomic sublevels, known as the Zeeman shift, comes about because of the interaction between the magnetic moment of an atom and that of an external field. The frequency shift of a level is

$$\Delta\omega = \frac{m_j g_j \mu_B}{\hbar}B, \tag{2.13}$$

where B is the magnetic field magnitude, m_j is the angular momentum quantum number, g_j is the Landé g factor, and μ_B is the Bohr magneton (see Appendix A for constants). This shift affects the energy of states, the frequency of the phase evolution of each state, and frequency of a transition to or from an affected level. For the resonant transition in Sr, only the excited state has $m_j \neq 0$, so the shift is just equal to the shift of the excited state. We account for this by replacing δ_l in the rate

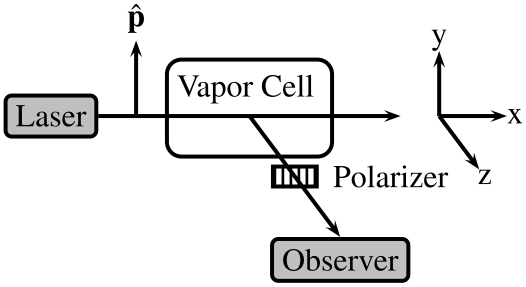

Figure 2.1 Hanle effect experiment measuring polaization

and saturation equations in Sec. 2.2 with an effective detuning that is the sum of the Zeeman shift, the laser detuning and, if applicable, the Doppler shift.

2.4 Polarization Hanle effect

The Hanle effect was discovered as a magnetic field dependent depolarization of light from atoms excited by resonant light [6, 12, 13]. While the effect we are interested is instead the directional dependence of the radiation, rather than the polarization, it will be helpful to first derive the case of polarization dependence in a simple setup, since the underlying physics is the same.

For the following derivation we assume an experimental setup as depicted in Fig. 2.1. A laser excites atoms in a fluorescence cell with a polarization $\hat{\mathbf{p}} = \hat{\mathbf{y}}$. The laser travels in the $\hat{\mathbf{x}}$ direction, and the observer views the fluorescence in a direction perpendicular to the laser travel and polarization, and parallel to the magnetic field vector, at a distance of z in the $\hat{\mathbf{z}}$ direction. We choose these coordinates because the natural coordinate system for dealing with the Zeeman shift is to align the z-axis with the B field. We can now simplify Eq. (2.1) and find that the radiation field seen by the

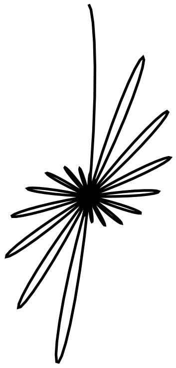

Figure 2.2 Motion of a decaying electron oscillation in a magnetic field.

observer, without a magnetic field present, is

$$\mathbf{E_r} = \frac{1}{4\pi\varepsilon_0}\frac{k^2 d}{z} e^{-i\omega t_r}\hat{\mathbf{y}}, \tag{2.14}$$

which is linearly polarized.

If we introduce a magnetic field, it will modify the polarization of this scattered light. For a classical dipole this is not surprising, as the Lorentz force would cause the dipole to rotate. Consider, for example, an oscillating electron in a perpendicular magnetic field. Qualitatively we would expect the electron's motion to look something like the damped Lissajous in Fig. 2.2 (not forgetting the damping discussed in Sec. 2.2). We could make such a classical argument quantitatively as well (the only nonclassical piece needed would be the damping constant, which comes from the lifetime of the energy state), but we will use a different approach.

Instead of modeling electron oscillations, we make an argument based on the Zeeman splitting of quantum levels in the atom. For this derivation we assume a simple two level atom, where the ground state has angular momentum $l = 0$, and the excited state has $l = 1$ and three magnetic substates. There are three corresponding transitions from the ground to excited states, σ^-, π and σ^+, for transitions to the $m = -1, 0$ and 1 states, respectively. Only the excited states with $m = \pm 1$ are affected by a magnetic field B. If we choose $\hat{\mathbf{z}} = \hat{\mathbf{B}}$, then the $\sigma^\pm$ transitions correspond to absorbing or emitting a photon of polarization $\hat{\mathbf{e}}_\pm$, so we decompose the polarization ($\hat{\mathbf{p}} = \hat{\mathbf{y}}$) into these components,

$$\hat{\mathbf{p}} = \frac{i}{\sqrt{2}}(\hat{\mathbf{e}}_- - \hat{\mathbf{e}}_+). \tag{2.15}$$

Utilizing the superposition principle, we then calculate the resulting emitted radiation field for each polarization component of the stimulating light, and add them together. The light coming from the two transitions is shifted separately, so they no longer have the same frequency ω. We call the shifted frequencies ω_+ and ω_-. Initially, the stimulated dipoles are along the same vector as the stimulating light polarization, so we'll plug the two terms in Eq. (2.15), along with $\pm\omega$, their corresponding shifted frequencies, into Eq. (2.1), the general radiation expression. The resulting radiation field is

$$\mathbf{E_r} = \frac{id}{2\sqrt{2}\pi\varepsilon_0}\left(\frac{k_+^2}{z}e^{-i\omega_+ t_r}\hat{\mathbf{e}}_- - \frac{k_-^2}{z}e^{-i\omega_- t_r}\hat{\mathbf{e}}_+\right)e^{-\gamma t_r}, \tag{2.16}$$

where $k_\pm = \omega_\pm/c$.

In the absence of a magnetic field ω_+ would be the same as ω_-. The resulting radiation from the two polarization components would cancel each other out in just the right way to give the overall radiation pattern, and polarization of a classical linear dipole. The Hanle effect comes about because the field shifts these levels slightly, just enough that the radiation fields from the two components drift out of phase with time, and no longer cancel each other out perfectly.

The phase difference grows with time, so we need to calculate the polarization of the radiation as a function of t_r. The result of this calculation will give us the intensity and polarization for a single atom as a function of time. Once we have this function we will need to sum over an ensemble of atoms excited at different times to get the overall intensity and degree of polarization seen by an observer.

The shift in energy is equal and opposite for the two, so we will substitute

$$\begin{aligned} \omega_L &= \frac{\mu_B}{\hbar} B \text{ (Zeeman shift)}, \\ \omega_+ &= \omega + \omega_L, \\ \omega_- &= \omega - \omega_L, \end{aligned} \tag{2.17}$$

where ω_L is the Zeeman shift, or Larmor frequency (not to be confused with ω_l, which is the laser frequency), remembering also the frequency dependence of the k's in the equation ($k_\pm = \omega_\pm / c$, $k = \omega / c$). Then we clean the result, and make the approximation that $\omega_L / \omega \approx 0$ in the amplitude (i.e. $k_\pm^2 \approx k^2$). After making all these substitutions, and pulling out common factors from the two terms we are left with

$$\begin{aligned} \mathbf{E}(r) &= -\frac{i}{4\sqrt{2}\pi\varepsilon_0} \frac{dk^2}{z} e^{-i\omega t_r} (e^{i\omega_L t_r} \hat{\mathbf{e}}_- - e^{-i\omega_L t_r} \hat{\mathbf{e}}_+) e^{-\gamma t_r} \\ &= -\frac{1}{4\sqrt{2}\pi\varepsilon_0} \frac{2dk^2}{z} e^{-i\omega t_r} (\cos(\omega_L t_r) \hat{\mathbf{y}} + \sin(\omega_L t_r) \hat{\mathbf{x}}) e^{-\gamma t_r}. \end{aligned} \tag{2.18}$$

The light then passes through a polarization filter oriented at an angle α to the original polarization. Treated separately, the $\hat{\mathbf{y}}$, and $\hat{\mathbf{x}}$ components of the field each pick up a factor of $\cos\alpha$ and $\sin\alpha$, respectively, and are rotated parallel to the polarizer. If we then rotate into the frame of the polarizer, the two terms add together along the same vector, so that

$$\mathbf{E}(r) \cdot \hat{\mathbf{m}} = -\frac{1}{4\sqrt{2}\pi\varepsilon_0} \frac{2dk^2}{z} e^{-i\omega t_r} (\cos(\omega_L t_r) \cos\alpha + \sin(\omega_L t_r) \sin\alpha) e^{-\gamma t_r}, \tag{2.19}$$

where $\hat{\mathbf{m}}$ is the direction of the polarizer. The resulting intensity on the detector, due to a single atom, is

$$\begin{aligned} I_{\text{atom}}(\alpha) &= I_H (\cos(\omega_L t_r) \cos(\alpha) + \sin(\omega_L t_r) \sin\alpha)^2 e^{-2\gamma t_r}) \\ &= I_H \cos^2(\omega_L t_r - \alpha) e^{-2\gamma t_r}, \end{aligned} \tag{2.20}$$

where $I_H = 2c\varepsilon_0 (dk^2 / (4\sqrt{2}\pi\varepsilon_0 z))^2$.

This is the intensity from a single atom excited at $t = 0$. In steady state we have to sum over N atoms, excited at a rate R, with equal probability of being excited at any time, making t_r anywhere

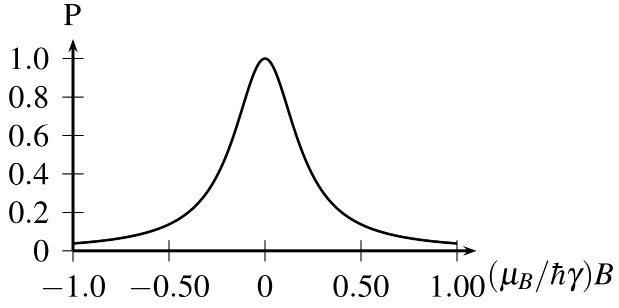

Figure 2.3 Polarization degree as a function of magnetic field.

between 0 and ∞ for each atom. We integrate over excited atoms in all stages of decay to obtain the total intensity on the detector:

$$\begin{aligned} I_d(\alpha) &= I_H RN \int_0^{\infty} \cos^2(\omega_L t'_r - \alpha) e^{-2\gamma t'} dt'_r \\ &= \frac{I_H RN}{4} \left(\frac{1}{\gamma} + \frac{\gamma \cos 2\alpha}{\omega_L^2 + \gamma^2} + \frac{\omega_L \sin 2\alpha}{\omega_L^2 + \gamma^2}\right). \end{aligned} \tag{2.21}$$

The expression above basically gives us the intensity of light coming through a polarizer (at angle α to $\hat{\mathbf{y}}$). If α is adjusted to find the polarization component with maximum intensity, then the minimum intensity will be 90° from that. From these values we can calculate the linear polarization degree P, which is the ratio of the difference of these two components to their sum, and is often the measured quantity in experiments using the Hanle effect. Using the max and min angles of polarization for small ω_L, $\hat{\mathbf{x}}$ and $\hat{\mathbf{y}}$ (i.e. $\alpha = 0, \pi/2$) we get

$$\mathrm{P} = \frac{1}{1 + \omega_L^2/\gamma^2} = \frac{1}{1 + (\mu_B^2/4\hbar^2\gamma^2)B^2}. \tag{2.22}$$

This function is shown in Fig. 2.3.

2.5 Directional Hanle effect

The derivation in the previous section shows how the polarization of light from an atom is affected by the presence of a magnetic field. In classical terms, the polarization changes because the field

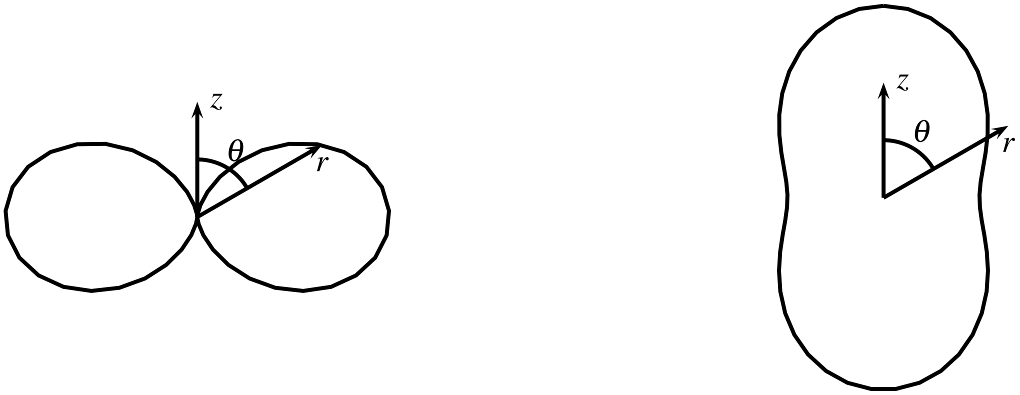

(a) Radiation pattern from a linearly oscillating dipole oriented with $\hat{\mathbf{z}}$

(b) Radiation pattern from a dipole along $\hat{\mathbf{e}}_{\pm}$ (i.e a dipole perpendicular to and rotating around $\hat{\mathbf{z}}$)

Figure 2.4 Dipole radiation patterns compared for linear or rotating dipoles of equal complex magnitude. The 3D radiation pattern is obtained by rotating each pattern around the z-axis. The resulting surfaces enclose equal volumes.

causes the oscillating dipole to rotate. This change in polarization is typically the observed variable in Hanle effect based measurements. Our method, on the other hand, is based on observing the change in directionality, rather than polarization, of the radiation.

Consider a dipole oscillating on a line pointing directly towards an observer. The observer sees no perpendicular acceleration in the charges making up the dipole, and detects no light. This is apparent from the dipole radiation patterns calculated in Sec. 2.1. The intensity radiation patterns for all three basis dipoles are symmetric around $\hat{\mathbf{z}}$. The intensity of a dipole oriented along $\hat{\mathbf{e}}_1$ goes as $\sin^2\theta$ and the intensity of the two circular polarizations have the same emission pattern, which goes as $\cos^2\theta + 1$. The resulting patterns for a dipole moment along $\hat{\mathbf{e}}_1$ or $\hat{\mathbf{e}}_{\pm}$ are shown in Fig. 2.4.

Now consider the effect of a magnetic field on the same case (an observer viewing a dipole along it's axis). The field will cause the dipole to rotate so that the observer does see acceleration in the component charges, and detects light coming from the dipole. In general, the patterns seen in Fig. 2.4 are going to be rotated by a magnetic field, giving off radiation all the while so the net result is the time average of the patterns as they rotate and decay. In a sense, the patterns are blurred

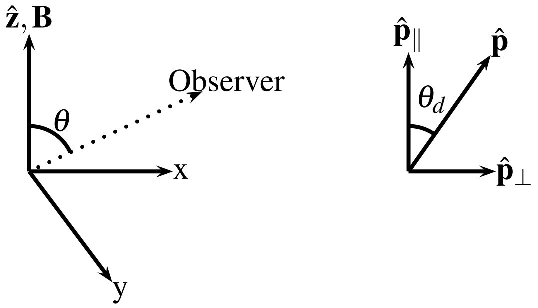

Figure 2.5 Directional Hanle effect coordinates

around the magnetic field, with intensity becoming more uniform in directions perpendicular to the field as it increases. We are interested in quantifying this effect for a general stimulating polarization and magnetic field.

The derivation will closely parallel that of the previous section, but the differences in geometry are important to note. The polarization is no longer assumed to be perpendicular to the observer or the field. We need a more general expression, so we will allow the angle of the observer and the polarization to be completely general relative to the magnetic field.

We can't align the axes with the field, polarization and the observer all at the same time anymore, since they are no longer at perpendicular angles. We will pick $\hat{\mathbf{B}}$ again to define the z axis, and allow the polarization and observation direction to be arbitrary. To begin, we will break the stimulating polarization $\hat{\mathbf{p}}$ into components parallel $\mathbf{p}_{\|}$ and perpendicular $\mathbf{p}_{\perp}$ to the magnetic field (see Fig. 2.5). We choose $\hat{\mathbf{z}}$ in the direction of $\mathbf{B}$ and $\hat{\mathbf{x}}$ in the direction of $\mathbf{p}_{\perp}$. These two field components stimulate an oscillating dipole moment $\boldsymbol{\mu}_{21} = \cos\theta_d \hat{\mathbf{z}} + \sin\theta_d \hat{\mathbf{x}}$, where θ_d is the angle between $\hat{\mathbf{B}}$ and $\hat{\mathbf{p}}$. We would like to find a general formula for outgoing intensity as a function of $\boldsymbol{\mu}_{21}$, θ and ϕ, where θ is the zenith angle, and ϕ the azimuthal angle in a standard spherical coordinate system defined in reference to the given Cartesian system.

The parallel portion of the stimulating light, $\mathbf{p}_{\|}$, will stimulate the π transition, and the resulting radiation field $\mathbf{E}_{\|}$ corresponding to the spontaneous emission of the $m = 0$ state is unaffected by the magnetic field. The answer to this portion is simply Eq. (2.1) with the first relation in Eq. (2.3):

$$\mathbf{E}_{\|} = -\frac{dk^2}{4\pi\varepsilon_0}\cos\theta_d \sin\theta \frac{e^{-i\omega t_r}}{r}\hat{\theta}. \tag{2.23}$$

Now we need to deal with the radiated field caused by the perpendicular component of the stimulating light, $\mathbf{p}_{\perp}$. To do so we will break it into circular components ($\hat{\mathbf{e}}_{+}$ and $\hat{\mathbf{e}}_{-}$) such that $\mathbf{p}_{\perp} = \sin\theta_d(\hat{\mathbf{e}}_{+} + \hat{\mathbf{e}}_{-})/\sqrt{2}$. Each of these $\hat{\mathbf{e}}_{\pm}$ components stimulates the corresponding $\sigma_{\pm}$ transitions, with a corresponding frequency $\omega_{\pm}$ that is Zeeman shifted away from ω_0. We'll make the same substitutions and approximations relating to $\omega_{\pm}$ as in Sec. 2.4. First, though, we'll look at the geometric term $(\hat{\mathbf{r}} \times \mathbf{d}) \times \hat{\mathbf{r}}$, which is more complicated in this case because the vectors are not strictly perpendicular. Plugging in Eq. (2.3), gives

$$\begin{aligned} (\hat{\mathbf{r}} \times \hat{\mathbf{e}}_{\pm}) \times \hat{\mathbf{r}} &= \frac{1}{\sqrt{2}}(\cos\phi\cos\theta\hat{\theta} - \sin\phi\hat{\phi}) \pm \frac{i}{\sqrt{2}}(\sin\phi\cos\theta\hat{\theta} + \cos\phi\hat{\phi}) \\ (\hat{\mathbf{r}} \times \hat{\mathbf{e}}_{\pm}) \times \hat{\mathbf{r}} &= \frac{A \pm iB}{\sqrt{2}}, \end{aligned} \tag{2.24}$$

where we've substituted $A = \cos\phi\cos\theta\hat{\theta} - \sin\phi\hat{\phi}$ and $B = \sin\phi\cos\theta\hat{\theta} + \cos\phi\hat{\phi}$ for simplicity. If we plug these two relations into Eq. (2.1), along with the time dependence, we get

$$\mathbf{E}_{\perp} = \frac{1}{4\pi\varepsilon_0 r}\frac{d}{2\sqrt{2}}((A + iB)k_{+}^2 e^{-i\omega_{+}t_r} + (A - iB)k_{-}^2 e^{-i\omega_{-}t_r})e^{-\gamma t_r}. \tag{2.25}$$

As in Sec. 2.4, we will substitute $k_{\pm} = \omega_{\pm}/c$, $\omega_{\pm} = \omega_0 \pm \omega_L$. We drop ω_L everywhere except in the complex exponential because it is very small compared to ω_0. In the exponential it acts as a time dependent phase shift between the two terms which does have a significant impact on the overall result. With a little rearranging this gives

$$\begin{aligned}
\mathbf{E}_\perp &= \frac{k^2}{4\pi\varepsilon_0}\frac{d}{2\sqrt{2}}e^{-\gamma t_r - iwt_r}(A(e^{i\omega_L t_r}+e^{-i\omega_L t_r}) - iB(e^{i\omega_L t_r}-e^{-i\omega_L t_r})) \\
&= \frac{k^2 d}{4\pi\varepsilon_0\sqrt{2}}e^{-\gamma t_r - i\omega t_r}(\underbrace{A\cos(\omega_L t_r)+B\sin(\omega_L t_r)}_{\begin{gathered}(\cos(\omega_L t_r)\cos\phi\cos\theta+\sin(\omega_L t_r)\sin\phi\cos\theta)\hat{\theta} \\ -(\cos(\omega_L t_r)\sin\phi-\sin(\omega_L t_r)\cos\phi)\hat{\phi}\end{gathered}}) \\
&= \frac{k^2 d}{4\pi\varepsilon_0\sqrt{2}}e^{-\gamma t_r - i\omega t_r}(\cos(\omega_L t_r-\phi)\cos\theta\,\hat{\theta}+\sin(\omega_L t_r-\phi)\hat{\phi}).
\end{aligned} \tag{2.26}$$

We're now ready to combine the parallel and perpendicular components and get that the radiation from a single excited atom is

$$\begin{aligned}
\mathbf{E_r} = \frac{k^2 d}{4\pi\varepsilon_0\sqrt{2}}e^{-\gamma t_r - i\omega t_r}[(\sin\theta_d\cos(\omega_L t_r-\phi)\cos\theta\ -\cos\theta_d\sin\theta)\hat{\theta} \\
+\sin(\omega_L t_r-\phi)\hat{\phi}].
\end{aligned} \tag{2.27}$$

The corresponding intensity is

$$I_{\text{atom}} = I_H e^{-2\gamma t_r}[(\sin\theta_d\cos(\omega_L t_r-\phi)\cos\theta-\cos\theta_d\sin\theta)^2+\sin^2\theta\sin^2(\omega_L t_r-\phi)], \tag{2.28}$$

where $I_H = c\varepsilon_0(k^2 d/8\pi\varepsilon_0)^2$. Remember that our field dependence is in ω_L, as $\omega_L = \mu_B B/2\hbar$.

As in Sec. 2.4, we need to multiply by N and integrate over t_r from 0 to ∞ to get the resulting steady state intensity from an ensemble of atoms. The result of this integration gets a little messy, so we'll leave this step for Sec. 4.1, where we derive the exact form of our model. Plugging in all the experimental parameters will simplify the expression above so that we can finish the calculation.

2.6 Rate dependence

The previous two sections on the Hanle effect make the assumption that the rate of spontaneous emission R is the same for all atoms in the ensemble and for each stimulated transition. This is approximately true if the stimulating light is a broad linewidth source, but is not true in our experiment with a narrow linewidth laser. We made the assumption in previous sections to get a simple analytical result, but we need to understand how much this assumption affects our results.

In Sec. 2.5, the rate dependence is buried in the overall amplitude of the radiation field, via the dipole moment magnitude d. The dipole moment is given in Eq. (2.11), and is proportional to the emission rate given in Eq. (2.9). The emission rate, however, depends on δ_l, which depends on both the Doppler and Zeeman detuning in any particular atom. We will account for this by replacing d^2 with $d_0^2 R_\pm(v,B)/R_0$, where $d_0 = \sqrt{6\pi\varepsilon_0 c^3\hbar k^3 R_0}$ and $R_0 = \Gamma I/I_s$.

This substitution first becomes significant in Eq. (2.25), because we can no longer completely factor the rate out of the $\omega_\pm$ terms. The modified result is

$$\mathbf{E}_\perp = \frac{1}{4\pi\varepsilon_0}\frac{d_0}{2\sqrt{R_0}}\left(\sqrt{R_+(v,B)}(A+iB)k_+^2 e^{-i\omega_+ t_r} + \sqrt{R_-(v,B)}(A-iB)k_-^2 e^{-i\omega_- t_r}\right)e^{-\gamma t_r}. \tag{2.29}$$

From there the math does not simplify as nicely because $\sqrt{R_+} \neq \sqrt{R_-}$, but in principle we could proceed in the same way: calculate the intensity per atom, then integrate over the ensemble of atoms. Our result now depends on the velocity, as well as t_r for a given atom, and while all t_r's were weighted equally, all v's should not be, so the integral averaging intensity over the ensemble changes to a double integral from $t_r = 0$ to $t_r = \infty$ and $v_0 = 0$ to $v_0 = \infty$, weighted with the Maxwell-Boltzmann distribution for the velocity spread, given by

$$N(v) = \sqrt{\left(\frac{m}{2\pi k_b T}\right)^3} 4\pi v^2 e^{-\frac{mv^2}{2k_b T}}. \tag{2.30}$$

The calculations become messy, so we did not attempt an analytical solution. The calculations can be done numerically for a particular problem, however, and we will show how including these rate effects influence our model in Chapter 4.

Chapter 3

Experiment

This chapter details the experimental methods used, including everything that is helpful or necessary to take the data that is presented and analyzed in the next two chapters. I will only give a brief overview of parts of our experiment that are well documented elsewhere [8], such as the vacuum systems.

3.1 Experiment

The experimental layout is basically the same as in Sec. 2.4, but with a few key changes. We measure overall intensity rather than polarization, and the stimulating polarization is towards the observer. Additionally, we image a region of the fluorescence, rather than a single point. Because of this, the observation angle varies a little over the are of the sensor. Depending on how far the camera is from the imaged region, this angle can be very close to parallel, which motivates the small-angle approximation made in the next chapter. See Fig. 3.1 for a schematic of the experiment in this chapter.

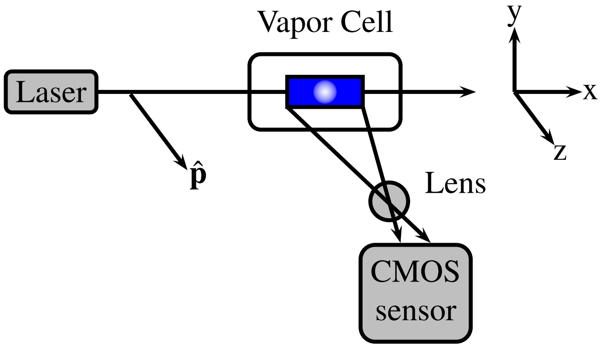

Figure 3.1 Directional Hanle effect experiment

3.2 Vacuum

The first necessary component in this experiment is a vapor cell. This is just a container for something that can fluoresce, which is strontium in our case. The stimulated emission must be dominated by natural relaxation from the excited state—not significantly influenced by collisions, for example. If we want to ignore collisions, this requires that the mean free time between collisions should be significantly greater than the excited state lifetime: $\tau_{\text{free}} \gg 1/\Gamma$.

We can estimate the vacuum necessary for this experiment by using some results from kinetic gas theory. We will assume a spherical collisional cross section with a radius d equal to the atomic radius, which is a broad oversimplification, but it is good enough to give us an idea of what we need. Alternatively, we could define the cross section as the distance at which the dipole interaction energy between two excited atoms is comparable to the transition energy, but this distance only differs from the atomic radius by less than a factor of two and doesn't effectively change the results of the following argument.

Using a mean free path, and velocity of

$$l = \frac{k_B T}{\sqrt{2}\pi d^2 P}, \quad v_{\text{rms}} = \sqrt{\frac{3k_B T}{m}},$$

respectively, where P is the pressure and T is temperature we get that

$$\tau_{\text{free}} \approx \frac{l}{v_{\text{rms}}} = \frac{1}{\pi d^2 p}\sqrt{\frac{k_{\text{B}} T m}{6}}.$$

With a temperature of 500° C (about where we keep our oven at for a strong fluorescence signal—background gases will be closer to room temperature, making this a worst case estimate), this restricts our vacuum pressure to

$$P << \frac{1}{\pi d^2 \Gamma}\sqrt{\frac{k_{\text{B}} T m}{6}} = 200 \text{ Torr}.$$

This is a fairly easy condition to meet. A stable MOT requires vacuum on the order of 10^{-7} Torr or better. Our vacuum system is designed for a MOT, and easily exceeds these requirements.

The motion of the atoms won't be a problem for imaging either. The lifetime of the transition is about 30 ns, during which time the atoms, moving on average at about 470 m/s at 500° C, will have moved 15 μm. A single pixel corresponds to a 120 μm square region on the imaged plane, so the signal from a single decay event won't wash over multiple pixels.

3.3 Strontium

Working with Sr is a little tricky. We found previously, for example, that standard glass vacuum windows would get coated with the Sr over time and become opaque. Using sapphire windows instead, and keeping them heated to $\sim 350°$ C seems to be a better long term solution. We use a sapphire viewport with a glass to metal seal on the window that atoms from the oven hit directly. The rest of the windows in the vapor cell are optically flat AR coated fused silica viewports with glass to metal seals from MPF Products Inc.

The Strontium itself comes in sealed glass ampoules. It oxidizes quickly, and the oxide is difficult to bake off, so we are careful to keep it from contact with air as much as possible. When the strontium in the oven needs to be replaced we first flood the MOT chamber with pure argon.

While maintaining positive argon pressure in the vapor cell we remove the Conflat (CF) sealed blank at the back of the oven and slide the strontium ampoule inside. The ampoule is then smashed using a long metal tool, and the larger glass pieces are removed. Then we reattach the CF blank and pump down the chamber. This must be done as quickly as possible once the Sr is exposed to avoid excessive oxidation.

Even taking the precautions above, the Sr is usually coated with enough oxide that there is a very low vapor pressure when it is first heated up. To overcome this we heat the Sr to over 700° C for a few minutes to get the oxide off. After doing this once, the oven usually needs to be heated to only 450° C - 500° C to get a high enough vapor pressure for experiments.

3.4 Laser

The laser we are using is a NewFocus Vortex Plus tunable diode laser. The laser uses a diode laser in an external cavity with a diffraction grating. The grating angle is controlled by piezos, and is the main way to scan the laser wavelength. The laser has a wavelength scan of about 0.2 nm centered on 460.7 nm for the laser. The power output varies between 30 mW-40 mW depending on current and grating angle. The current generally needs to be adjusted with grating angle changes to optimize the power for a given wavelength. Without any feedback control the passive drift of the device is around 10 MHz/hour. This is more than stable enough for our experiment since it is less than Γ, which is in turn much less than the width of the Doppler profile in our atom beam. In other words, this shift is equivalent to about a 5 m/s Doppler shift, and the velocity distribution of our atoms is relatively flat on that scale.

The spatial mode of the laser is usually close to Gaussian, depending on the laser parameters. To insure a predictable and consistent mode, we focus the laser through a pinhole 5 μm in diameter. This ensures an approximately Gaussian mode, but does cost a few mW of power.

3.5 Imaging

Imaging is done with a webcam because it is inexpensive, simple to use, and meets our needs. A scientific camera could potentially give better results due to lower noise, more linear response, etc. We use a Logitech QuickCam®Pro 9000 PC webcam, because it has been used and studied for scientific imaging [14, 15], and has an active community of advanced users [16].

The webcam has a CMOS sensor with a resolution of 1600x1200 pixels, and costs around $50. As with most consumer cameras, the CMOS sensor is covered with a checkerboard pattern of green, red and blue filters, called a Bayer filter. Internal processing algorithms extrapolate the color at each pixel from the neighboring pixels with the appropriate filter over it. To use such a sensor we need to disable any such internal imaging processing, and select a subset of pixels with a single filter—in our case the blue pixels since they give the highest signal.

The Logitech webcam can be put in a raw data mode using the bayer.exe [17] executable provided by Logitech engineers, at which point it gives the raw CMOS sensor values before any software filtering is done. The result is a checkerboard pattern due to the Bayer filter pattern. Once the subset of blue filtered pixels is selected, a smooth image for fitting and analysis is available.

Chapter 4

Numerical Analysis

The purpose of this chapter is to find a model based on the directional Hanle effect theory from Sec. 2.5 that describes the data taken from our camera. We need such a model so we can fit the data to the model, and extract some useful information from the fit parameters. Because the fluorescence response and the camera response are both assumed to be linear, the model just needs to account for the shape of the intensity dependence, and not the overall magnitude—the intensity scale can be included as a fitting parameter, which means we don't need to worry about calibration of our sensors.

The physical quantity we would like to observe is the magnetic field. In particular, we would like to extract the zero-point of the field (x_0, y_0), and its gradient through the zero-point. The model for the digital pixel values in a data sample must be of the form

$$F(x, y; \text{parameters})$$

where x and y are coordinates on the plane imaged onto pixel (i, j), and 'parameters' is a list of fitting parameters to be determined. If the gradient can be determined by just the 2D data, then there should exist functions G_x, and G_y such the gradients of the x and y components of the field are given by

$$\begin{aligned} G_x(\text{parameters}) &= \frac{\partial B_x}{\partial x} \equiv b_x \\ G_y(\text{parameters}) &= \frac{\partial B_y}{\partial y} \equiv b_y, \end{aligned} \tag{4.1}$$

where we've defined b_x and b_y to be the gradients of the x and y components of the field along the x and y axes, respectively. Similarly, $b_z \equiv \partial B_z/\partial z$. For the model we will assume a simple linear field given by

$$\mathbf{B} = b_x(x-x_0)\hat{\mathbf{x}} + b_y(y-y_0)\hat{\mathbf{y}} + b_z(z-z_0)\hat{\mathbf{z}} \tag{4.2}$$

which is approximately true close to the center of our trapping fields. This parameterization gives easy access to the key field characteristics which we care about for atom trapping—that is, the position (x_0 and y_0), and the gradient (b_x, b_y and b_z).

The first three sections of this chapter are dedicated to finding the functional forms of F, $G_{x,y}$, and their corresponding list of parameters. Once these are found, we can fit the data to the model and extract the field gradients (i.e. b_x and b_y) from the resulting fit parameters. A single 2D image allows us only to extract two of the gradient values, but $b_z = b_x$ due to symmetry of the field, so that is all we need. The last section will discuss the numerical methods used to do the data fitting.

4.1 Model

The signal chain for the pixel value we read from the camera is as follows: the pixel value depends on the incident intensity, which in turn depends on the stimulated intensity at the spot imaged, which in turn depends on the intensity of the stimulating light. Each step in this chain is linear in intensity (assuming $I << I_s$, and we're operating in the linear range for the sensor), so if we can find the response for each of these stages, and the initial stimulating intensity, then the function we are looking for is simply the product of these stages.

First then, we will account for the intensity of stimulating light at the point in space imaged onto a pixel. We assume the spatial mode of the laser is approximately Gaussian, collimated over the imaged region, and is centered on a slit so the beam is a 2D sheet. The intensity profile looks like

$$I_l(x,y) \propto e^{-y^2/w^2}, \tag{4.3}$$

where w is defined as the beam radius.

Now, using Eq. (2.28) we can determine the relative fluorescence response. If the sheet of light is centered on (x_0, y_0, z_0) in lab coordinates (i.e. it is passing directly through the field zero-point), and is oriented in the x,y plane, then the z component of the magnetic field is zero throughout the imaged region due to the symmetry of our fields. In other words the magnetic field is purely in the lab's xy plane, and is always perpendicular to the polarization, so only the $\sigma_\pm$ transitions are stimulated. We need to translate coordinates and vectors into the atom's frame, as defined at the beginning of Sec. 2.5, and which we will denote here as $\hat{\mathbf{x}}'$, $\hat{\mathbf{y}}'$, and $\hat{\mathbf{z}}'$. The atoms are all on the xy plane of the lab frame, but spread over the imaged region, so there is a translation of the origin as well as a rotation to consider when transforming vectors or points to an atoms frame. Since the polarization is purely in the $\hat{\mathbf{z}}$ direction, the coordinate transformation is as follows: $\hat{\mathbf{x}}' = \hat{\mathbf{z}}$, $\hat{\mathbf{z}}' = \hat{\mathbf{B}} = \cos\theta\hat{\mathbf{x}} + \sin\theta_B\hat{\mathbf{y}}$ and $\hat{\mathbf{y}}' = \hat{\mathbf{z}}' \times \hat{\mathbf{x}}' = \sin\theta\hat{\mathbf{x}} - \cos\theta\hat{\mathbf{y}}$. With this we construct the rotation matrix[1]

$$\mathbf{R}(x,y) = \begin{bmatrix} 0 & 0 & 1 \\ \sin\theta_B & -\cos\theta_B & 0 \\ \cos\theta_B & \sin\theta_B & 0 \end{bmatrix} = \frac{1}{B}\begin{bmatrix} 0 & 0 & B \\ b_y y & -b_x x & 0 \\ b_x x & b_y y & 0 \end{bmatrix}, \tag{4.4}$$

from which we can transform any vector from the lab frame coordinates system to the atom's.

The relevant variables in Eq. (2.28), are θ_d, θ, and ϕ. Because $\hat{\mathbf{p}} = \hat{\mathbf{z}}$ is always perpendicular

---

[1] This matrix follows directly from the equations in the previous sentence relating the two basis, but it can also be derived by making three rotations to correctly align the axes with the primed coordinates. One is by an arbitrary angle θ_B but the other two are by set angles and have a simple form.

to **B**, $\theta_d = \pi/2$, simplifying Eq. (2.28) to

$$I = I_0 e^{-2\gamma t_r}[\cos^2(\omega_L t_r - \phi\cos^2\theta) + \sin^2(\omega_L t_r - \phi)]. \tag{4.5}$$

Integrating over t_r (see Sec. 2.4 and 2.5), we are left with a radiation intensity of

$$I_r(\theta,\phi) = \frac{I_0 RN}{8}\left(\frac{\cos(2\theta)}{\gamma} + \frac{3}{\gamma} - \frac{2\sin^2(\theta)\,(\gamma\cos(2\phi) + \omega_L\sin(2\phi))}{\gamma^2+\omega_L^2}\right) \tag{4.6}$$

Now we just need θ and ϕ as functions of x and y. If we write the observation point as $(0,0,L)$ in lab coordinates, then we translate by $(-x,-y,0)$ and rotate to get that the observation point in atom coordinates is

$$\mathbf{R}\cdot\begin{bmatrix}-x\\-y\\L\end{bmatrix} = \frac{1}{B}\begin{bmatrix}LB\\(b_x-b_y)xy\\-b_x x^2 - b_y y^2\end{bmatrix} = \frac{1}{\sqrt{g_x^2x^2+g_y^2y^2}}\begin{bmatrix}L\sqrt{g_x^2x^2+g_y^2y^2}\\(g_x-g_y)xy\\-g_x x^2 - g_y y^2\end{bmatrix},$$

where we've defined the fitting parameters $g_x = (\mu_B/2\hbar\gamma)b_x$, and $g_y = (\mu_B/2\hbar\gamma)b_y$. From this we extract the polar coordinates

$$\begin{aligned}\theta &= \tan^{-1}\left(-\frac{\sqrt{L^2(g_x^2x^2+g_y^2y^2)+(g_x-g_y)^2x^2y^2}}{g_x x^2+g_y y^2}\right)\\ \phi &= \tan^{-1}\left(\frac{(g_x-g_y)xy}{L\sqrt{g_x^2x^2+g_y^2y^2}}\right).\end{aligned} \tag{4.7}$$

Now we can combine Eq. (4.3) and Eq. (4.6), pull out a factor of $1/\gamma$ and combine it with the other pre-factors into another fitting constant A. Then we do a little algebra to turn all the ω_L's and γ's into $g_{x,y}$'s. The result is our fitting model for the image data:

$$F(x,y;A,w,g_x,g_y) = A e^{-y^2/w^2}\left(\frac{3}{2} + \frac{\cos(2\theta)}{2} - \frac{\sin^2(\theta)\left(\cos(2\phi)+\sin(2\phi)\sqrt{g_x^2x^2+g_y^2y^2}\right)}{1+g_x^2x^2+g_y^2y^2}\right). \tag{4.8}$$

The fitting parameters are A, w, g_x and g_y, and the functions that give the gradients—$G_{x,y}(\text{parameters})$—turn out to only depend on the $g_{x,y}$ parameters, and are linear with respect to them. The field gradients are given by

$$b_{x,y} = \frac{2\hbar\gamma}{\mu_B} g_{x,y}. \tag{4.9}$$

It's a little ugly to look at, but the computer handles it just fine.

4.2 Small-angle approximation

We can make some reasonable geometric approximations that will give us a more manageable analytical solution. This basically comes down to making the small-angle approximation for the angle between the vectors from the observer to the zero-point of the magnetic field and the observer to the field point, which is true so long as the distance from the camera to the observed region is large compared to the width or height of that region. Assuming the camera is far enough away, such that $L^2 \gg x^2 + y^2$, we make the approximations $\theta \approx \pi/2$, and $\phi \approx 0$, which gives

$$I_r(x,y) = \frac{2I_0RN}{8\gamma}\left(1 - \frac{1}{1+g_x^2x^2+g_y^2y^2}\right). \tag{4.10}$$

Combining this result with the Gaussian beam shape from Eq. (4.3), our overall geometric approximate fitting model becomes

$$F(x,y;A,w,g_x,g_y) \approx Ae^{-y^2/w^2}\left(1 - \frac{1}{1+g_x^2x^2+g_y^2y^2}\right). \tag{4.11}$$

The x and y profiles through the center of the model function are shown in Fig. 4.1. Note that, having approximated away all the geometric effects, we are left with the same kind of Lorentzian shape that we derived in Sec. 2.4 as the basis for our model.

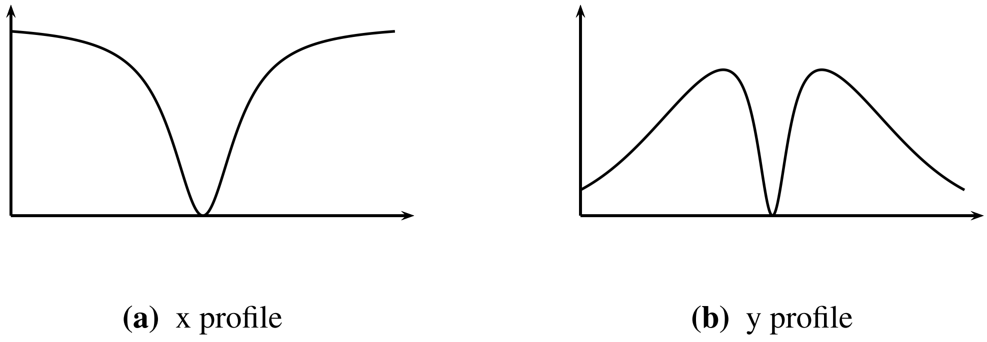
(a) x profile **(b)** y profile

Figure 4.1 Profile plots showing the general shape of the model through (a) a cross-section with $y = 0$ and (b) a cross-section with $x = 0$. This includes the overall Gaussian shape of the laser beam seen in the y profile.

4.3 Including rate effects

We can improve the analytical results for the small-angle approximation by doing a numerical calculation that includes the rate imbalance between $\sigma_\pm$ transitions, and the difference in stimulation rate for atoms at different velocities. We do so by evaluating Eq. (2.29) on the polarization axis in our experiment and following the procedure outlined in the paragraph after it—that is, we find the intensity, then do a numerical integral over t_r and v. We do this with a set of magnetic field, B, and saturation parameter, $s_0 = I_0/I_s$, values to get a dataset representing the on axis intensity $I_{\text{axis}}(B, s_0)$.

The results of this numerical calculation are shown in Fig. 4.2, where they are compared to our analytical small-angle Lorentzian model, Eq. (4.11). Notice that including the rate effects makes only a small difference. For larger saturation values, especially, the curve is very close to the analytical solution we developed before. This makes sense because saturating a transition broadens the absorption profile, which has similar results to broadening the stimulating light profile, and our analytical results are accurate in the limit of a flat intensity profile of the stimulating light.

It is more difficult to explain why the $I_{\text{axis}}(B, s_0)$ curve is close to the approximate solution for low s_0 values, but we can give a simple conceptual argument. The reason why we might expect a

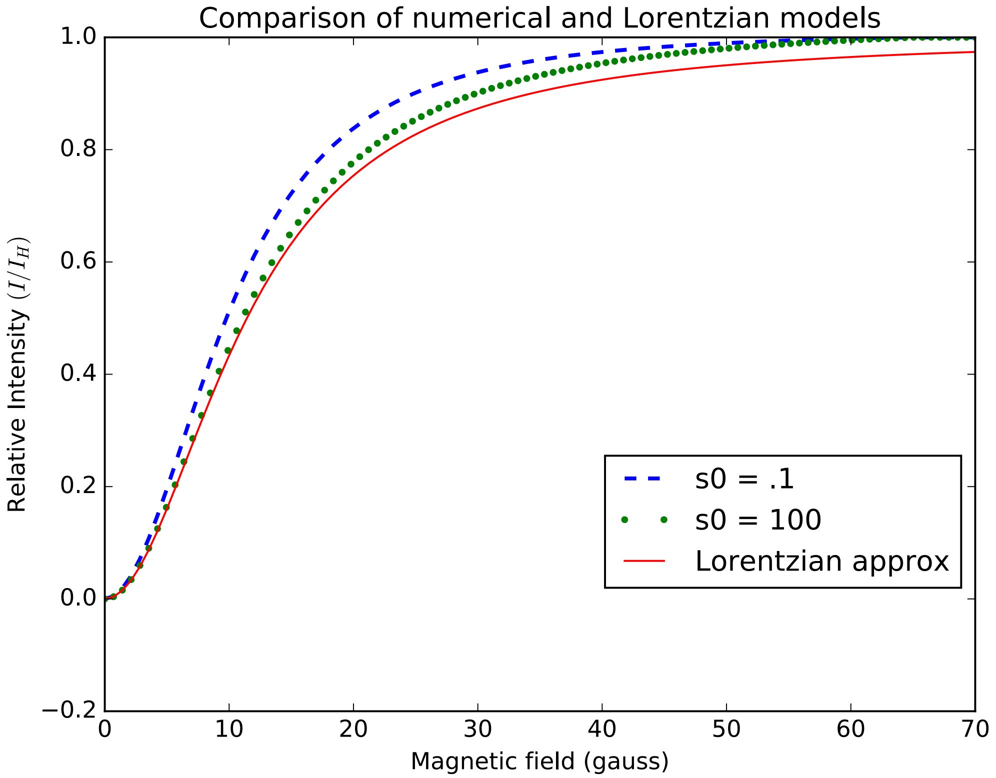

Figure 4.2 Three curves comparing the amount of light emitted along the polarization axis for. The first two show the numerical calculations for low and high saturation values that include changes in emission rate with the Doppler and Zeeman effects, and the third shows the analytical model (Eq. (4.11) plotted vs $B = g_x^2 x^2 + g_y^2 y^2\ B$, instead of x and y), which is approximately correct for broadband stimulating light sources.

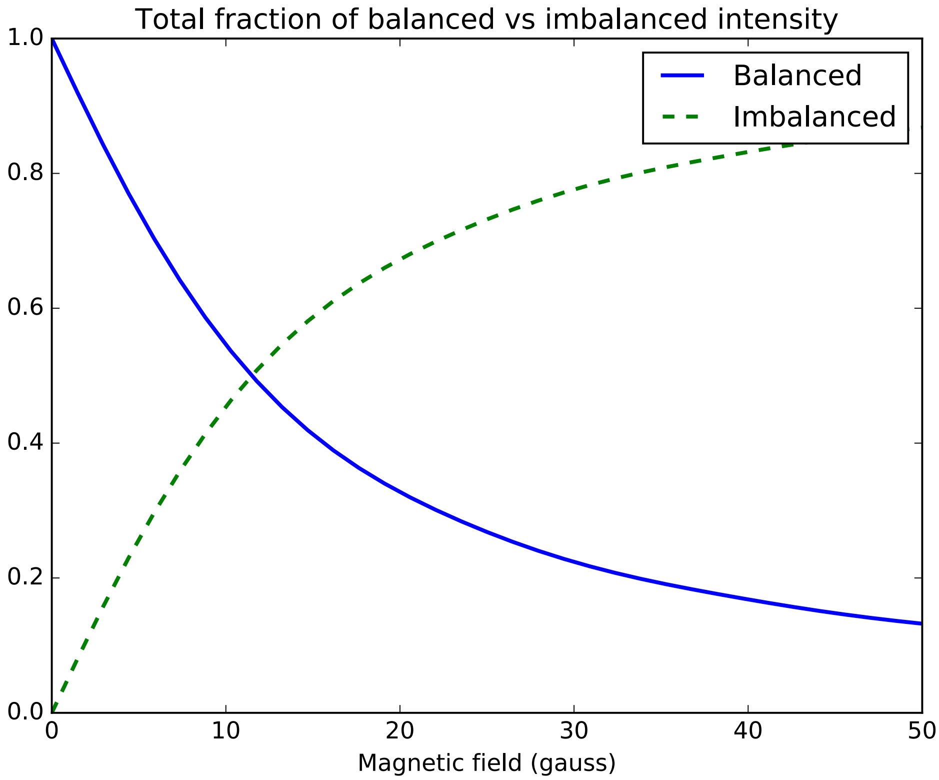

Figure 4.3 Ratio of balanced to imbalanced intensity as a function of magnetic field, where 'balanced' intensity the fraction of the overall spontaneous emission that comes from both transitions equally.

bigger difference when including rate effects is because the amount of rate imbalance is not small. Figure 4.3 shows the average imbalance of light emitted by $\sigma_{\pm}$ transitions in our ensemble, and the imbalance is clearly significant at low field values (less than 30 G, i.e. within the dip portion of the Lorentzian like curve). This indicates the imbalance in rate could cause a significant effect.

To understand why our results are only slightly affected we note that there are two effects that partially cancel each other out. The first is the rate imbalance between the two transitions, which becomes significant at relatively low field values (less than 30, i.e. within the dip portion of the Lorentzian like curve). The average rate imbalance vs magnetic field is show in Fig. 4.3

The rate imbalance effect ultimately results in a narrowing of the Lorentzian like $I_{\text{axis}}(B, s_0)$

curve. As long as there is an imbalance, then the light emitted by one transition will not completely cancel out the light emitted by the other transition on the polarization axis. This causes more light to be emitted on axis at a given field value than in our analytical calculations.

The second effect, however, causes a broadening of the Lorentzian like curve. This effect is the decrease in overall intensity emitted by the atom as a function of field. The majority of atoms in our ensemble are close to zero detuning from the stimulating light, so as the Zeeman splitting increases, both transitions experience a net detuning and a decrease in the scattering rate. In the absence of the previous effect we would expect this to broaden the $I_{\text{axis}}(B, s_0)$ curve, as well as lower the asymptotic limit.

To take these effects into account in our data analysis, we build an interpolated function from our numerical data to replace Eq. (2.29). The full numerical result depends on the saturation parameter as well as the field value, so we calculated curves for saturation parameters of .01, .1, 1 and 10, as well as field magnitudes of 0-60 G. This data is used to generate a 2D interpolated function that can replace Eq. (4.11) (though it needs additional input, $s_0(x, y)$). The interpolation is done with a bivariate spline that uses first order interpolation along the s_0 axis and 2nd order interpolation along the B axis.

4.4 Numerical methods

The data we have are stored in an image, i.e. a two dimensional array of values proportional to intensity. The model should fit those values if we find the right parameters. We just need to numerically find the best fit, which we will define as the set of parameters that gives the smallest average square deviation from the data, commonly known as a least squares fit. Most numerical computing packages include optimized functions for quickly finding such a fit for a set of data. We are using the open python computing platforms *NumPy* and *SciPy* [18, 19], which provide an optimized least squares fitting algorithm. These packages also provide numerical integration and interpolation, which are used for the numerical model including rate effects—the interpolation function is generated using the RectBivariateSpline() function from the interpolate module of *SciPy*.

In addition to the parameters defined by the model in Sec. 4.2, we will allow for offsets (e.g. if the camera is imperfectly aligned) by replacing x and y in the Lorentzian part of the model with $x - x_0$, $y - y_0$, respectively, and y in the Gaussian with $y - y_l$ to account for imperfect alignment of the laser. The x_0, and y_0 parameters should correspond to the exact zero-point of the magnetic field in the image.

Further corrections can be made for imperfect alignments by adding additional fitting parameters, so long as the parameter affects the overall result in a way that is distinguishable from other fitting parameters. For example, if the camera is rotated around it's viewing axis slightly, or the probe beam is at a slight angle, then this can easily be added to the model by rotating the image. Adding such a correction made little difference in the final results, so we keep only the x_0 and y_0 corrections here.

In practice, y_l, x_0 and y_0 can all be set manually with reasonable accuracy. If the beam is aligned properly and the view window centered on the dark spot in the fluorescence, then they are all close to the center point of the image. We'll leave them in the model to account for imperfect alignments. They don't significantly impact the speed of the fitting algorithm.

The library algorithm we use is designed for 1D functions of n variables. To fit to a 2D function, we just need to map our data and model to one dimension. We do so by stacking or unfolding the rows or columns of the 2D data matrix to a 1D list, and find an appropriate parametric function of one variable, t, for the x and y values corresponding to each data point in the 1D matrix. Then we can change our 2D function to a 1D function as $F(x,y) \to F(t) = F(x(t), y(t))$. Any such mapping should work fine, but the one we use is to unfold the rows of pixels like an accordion, so that two locations on the 1D array that are next to each other are always next to each other in the 2D picture as well. This isn't necessary, but it avoids discontinuities that could affect some fitting algorithms. As a function of the parametric, and discrete variable t we get

$$\begin{aligned} x &= \begin{cases} \mathrm{mod}(t,W)\mathrm{PX} - W/2, & \text{if floor}(t/W)\text{is even} \\ W/2 - \mathrm{mod}(t,W)\mathrm{PX}, & \text{if floor}(t/W)\text{is odd} \end{cases} \\ y &= \mathrm{floor}(t/W) \times \mathrm{PX} - H/2, \end{aligned} \tag{4.12}$$

where PX is the size of a pixel in the image, the W the width of the image, and H is the height.

After wrapping the 2D model in a 1D function (as explained above), we simply feed the function, a set of initial guesses, and the image data into the curve_fit() function from the scipy.optimize module, and the function calculates the optimal parameters. Using Eq. (4.9) we then extract the values of the magnetic field gradients. See Appendix C for more details on the code.

Chapter 5

Results

5.1 Data

The magnetic field we are using for the MOT is generated with a pair of permanent magnetic rings, rather than the more common technique using an pair of anti Helmholtz coils. This arrangement generates a radially symmetric field that goes to zero at the center of the coils, and again along a circular ring centered on the first zero-point and midway between the two magnets. This is depicted in Fig. 5.1a, which shows a numerical simulation of the field of such a setup in a 2D dimensional slice through the axis. The figure is colored according to the magnitude of the magnetic field so it is easy to see where the field goes to zero. In an experimental setup as described in Sec. 2.5, we would expect to see dark spots in the fluorescence from the Sr atoms at each of these zero-points. This is indeed what we get. Figure 5.1b is an image taken of the strontium fluorescence, and the three zero-points are clearly visible. Note that the two points on the side are off center, however, which is a good indication that the magnets are imperfectly balanced.

The point we care about for trapping is the zero on the symmetry axis at the center. If we zoom in on this spot and fit the image as described in Sec. 4.1, then we find that the field gradients are

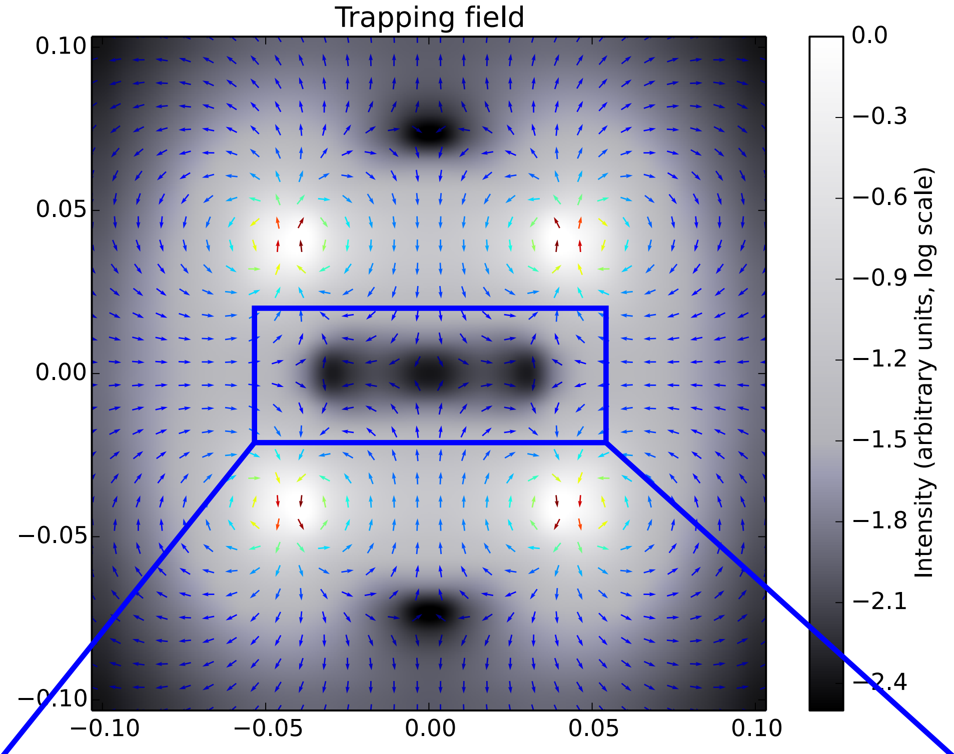

(a) Calculated magnetic fields on plane through magnet axis.

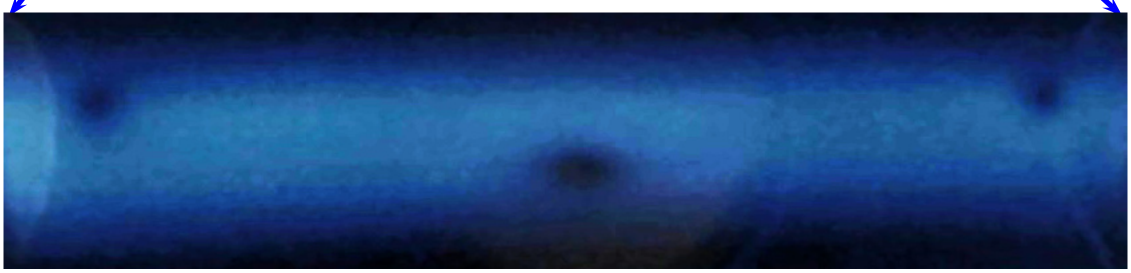

(b) Raw image data.

Figure 5.1 Zero-points of the magnetic field. Top: a theoretical plot of the magnetic vector field with a density map indicating overall field strength. Bottom: Data showing three dark spots due to the directional Hanle effect visible at three zero-points in the magnetic field in the plane of the light sheet (the zero-points on the sides are part of a ring of zero field around the center). Note the asymmetry visible due to imperfectly balanced permanent magnet strengths.

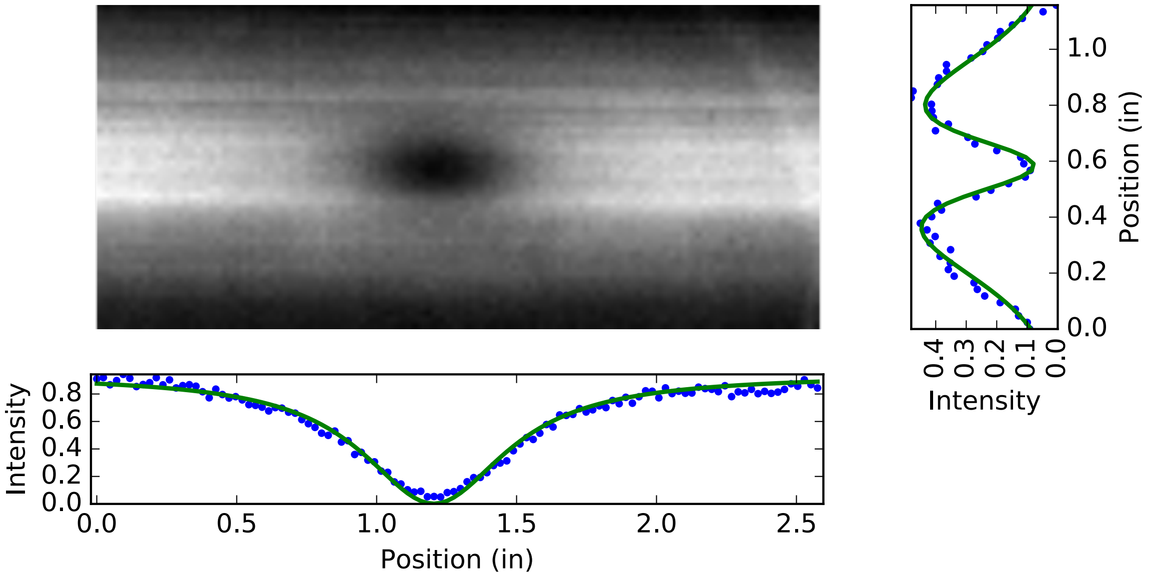

Figure 5.2 Image of the dark spot corresponding to the zero-point in our trapping potential, along with profile plots of the image (blue dots) and the model fit (green curves).

around $B_x = 36$ G/cm, and $B_y = 70$ G/cm, depending on which model we use (see Sec. 5.3). Fig. 5.2 shows this area in better detail, as well as profile plots along the x and y axis of the original image and the fit data.

These gradient values seem reasonable. We expect, from Maxwell's laws, that $B_x + B_y + B_z = 0$, and from the symmetry of the problem $B_x = B_z$, which means that $B_y = -2B_x$. The values we found satisfy this requirement to better than a few percent.

5.2 Independent gradient estimates

We verified our measurement of the axial gradient (i.e. B_y) using two other independent estimates. The first is based on measurements done with a Hall effect probe. It is impossible for us to measure the field in situ with this method, but we did measure each of the permanent magnets in isolation. The data from this measurement are a list of field values along the axis at regular intervals from the surface of the magnet. From this data we constructed an interpolated function of field strength on axis as a function of distance. By measuring the distance between the two magnets and adding the two interpolation functions together, we estimate the location and gradient of the zero-point between them.

The second value was determined by assuming the strength of both magnets was at the specified N42 magnet strength level, and using the corresponding surface current of 1.04×10^6 A/m in a simple numerical model of the magnet configuration. This value does not depend on the Hall probe measurement, so it is a good check, but is not expected to be as accurate, since we know there is some imbalance in the magnetization of the two ring magnets. It also suffers from the same potential error in the measurements of the geometry of the magnet setup.

5.3 Comparison of methods and approximations

The gradient values we calculate from the given data vary slightly depending on which approximation we use. Results from three different models are show in table 5.1, along with the two alternate axial gradient (B_y) estimates. The three models are the analytical model without rate effects (Eq. (4.8)), the small-angle approximate analytical model without rate effects (Eq. (4.10)), and the small-angle approximate numerical numerical model that includes rate effects. Two different results for the calculation from the numerical model are shown because a procedural error when the experiment was performed introduced uncertainty in the saturation parameter. We estimate that the parameter was between .1 and 1, and results assuming s_0 values on both edges of this range are shown for completeness sake. This uncertainty does not affect the analytical models because they assume equal rates in the $\sigma_\pm$ transitions such that saturation effects cancel.

In our setup the camera is far enough from the imaged region that the gradient values obtained from using the small-angle approximation versus the full geometric model vary from each other by

Model	B_x (G/cm)	B_y (G/cm)
Analytic (no geometrical approximations, no rate effects)	$35.80 \pm .29$	$70.27 \pm .51$
Analytic (small-angle approximation, no rate effects)	35.95 ± 0.29	$70.51 \pm .52$
Numerical (small-angle approx., includes rate effects, $s_0 = .1$)	$32.43 \pm .024$	$63.20 \pm .45$
Numerical (small-angle approx., includes rate effects, $s_0 = 1$)	$35.58 \pm .28$	$67.70 \pm .50$*
Hall probe measurement	—	67.3*
Permanent magnet simulation	—	69.0

Table 5.1 Tabulated results. The first two rows show results calculated using the analytical models, the third and fourth rows shows results using the interpolated numerical model with two different values for the saturation parameter, and the last two rows show values predicted by independent measurements. *The most accurate result should be from the numerical model (which uses the most complete theory), and the more accurate of the predicted values should be the Hall probe based calculation.

less than 2%. This lends credibility to the small-angle approximation. The most accurate results should be from the numerical model, which used the small-angle approximation and included effects from Doppler and Zeeman shifts across the velocity distribution. No attempt was made to numerically account for both the rate effects and deviations from the small-angle approximation, because it would make the numerical calculations much more complex and time consuming, and would have little effect.

When using the full geometric model from Eq. (4.8), there is an interesting effect due to the linear $\sin(2\phi)$ term that breaks the symmetry in the sign of B_x and B_y, so that we get slightly different values depending on whether we start the fit with g_x negative and g_y positive, or vice versa. If the data and fit are good enough, then it's possible this difference could be used, for example, to determine the appropriate sign of $B_{x,y}$ in addition to its magnitude. The difference is too small in our case to draw any reliable conclusions.

We also tested a slightly simpler 1D fit by fitting the approximate model to just one row of data for the x gradient and 1 column of data for the y gradient. With an initial guess for the row and column that are centered on the zero-point, we find a fit, then update the row and column according to the fit x_0 and y_0 values, to be closer to passing through the zero-point and fit again. The results of this one dimensional fit were within about 2% of the 2D fit. We don't seem to gain much by using the 2D fit, in this case, because there are enough pixels in a single row or column to still get good results.

5.4 Error

The expected value for the gradient (based on the interpolated magnet data) and the measured value with the directional Hanle effect (using the numerical model) agree to within 3%. It's difficult to say exactly how accurate the directional Hanle measurement is, however, because of the uncertainty in the saturation parameter, and because the only way we have to verify the results is the Hall probe measurement, which is not very precise.

The predicted value based on the Hall probe measurement has several sources of error. The measurement itself was done by hand, which means the spatial measurements (how far from the surface, and how far from the axis) are only accurate to about ±2 mm. (This measurement wasn't originally intended to be very precise, but it is impossible to redo it with the magnets in place). Additionally, the predicted value is very sensitive to the separation of the magnets in the cooling setup. A difference of ±10 mm corresponds to a factor of two difference in either direction. The separation of the magnets is known to ±1 mm, but the mechanical setup makes it difficult to guarantee they are coaxial to better than ±5 mm.

The field in the setup may also be modified by nearby heat sources which can weaken the magnet over time if it gets too hot. Most of the surrounding material and the vacuum chamber itself are not ferromagnetic, so the fields shouldn't be affected much by them. Altogether, predicting the gradient from measurements of the magnets and their setup is enough to get an idea of what to expect, but it is not a very reliable prediction.

The measurement from the Hanle effect has fewer sources of significant known error. The sensor should be linear unless close to saturation, so that shouldn't be an issue. Fitting to the 2D picture, as well as averaging over multiple video frames means the model is fit to thousands of data points, so any noise from the imaging system, if randomly distributed, should average out. The gradient does not significantly change when deliberately misaligning the polarization by $\pm 1^\circ$, and we can reliably set it to that accuracy.

5.5 Conclusion

The results presented above, as well as success with the alignment method detailed in Appendix B demonstrate that the Hanle effect can be a useful tool in cold atom experiments by giving the researcher a way to measure properties of the trapping field in situ. The position of the field zero-points can be easily determined, using this method, to within a fraction of the width of the fluorescence dark spots, which are on the order of $2\hbar\gamma/(\mu_B|\nabla\cdot\mathbf{B}|)$. This provides a very simple way to see the zero-point and adjust the field or the cooling lasers to perfect alignment. The gradient can also be determined with reasonable accuracy, which is useful for predicting trap properties. For a rough estimate, a simple Lorentzian fit is sufficient. If more information about the field is needed, this method could also be used to map the field out in regions where it is close to zero.

Appendix A

Useful constants

Table A.1 Physical Constants

Constant	**Symbol**	**Value**	**Dimension**
Electric vacuum permittivity	ε_0	$8.854 \times 10^{-}12$	$\mathrm{F\,m^{-1}}$
Bohr magneton	μ_B	9.27401×10^{-24}	$\mathrm{A\,m^2}$
Boltzmann constant	k_B	1.38065×10^{-23}	$\mathrm{J\,K^{-1}}$
Planck constant	h	6.62607×10^{-34}	J s
Reduced Planck constant	$\hbar$	1.054572×10^{-34}	J s

Table A.2 Properties of the strontium resonant transition, $5s^2 \rightarrow 5s5p$.

Constant	**Symbol**	**Value**	**Dimension**
Wavelength	λ	460.7331	nm
Natural linewidth	Γ	201	MHz
Dipole matrix element	μ_{21}	2.6354×10^{-29}	C m
5s5p landé g factor	g_j	1	
5s5p angular momentum	m_j	-1,0,1	
$5s^2$ angular momentum	m_j	0	

Appendix B

MOT alignment procedure

One simple, but helpful application of the directional Hanle effect described above, is an alignment procedure for MOT cooling beams. A typical MOT consists of three retro-reflected and mutually perpendicular laser beams, as well as a pair of field producing coils with the MOT chamber in between. The lasers must all cross at the same spot, which must overlap the zero-point of the magnetic field. If there is sufficient optical power, the beams can be made large enough that they can be aligned by eye initially. The coils are symmetric enough that the zero-point of the field is close to the center of the setup. When the MOT first forms, there is visible feedback to adjust beams or coils to more perfectly align everything and optimize the trap.

We found that using permanent magnets, the field is not as well balanced, and it is difficult to predict or adjust exactly where the zero-point of the field is. We also have limited optical power available, and need to concentrate it into smaller beams. The resulting beam width is much smaller than the area where the field zero-point could be. In addition, the smaller beam size makes it difficult to reliably align the lasers so they all cross at a single point inside the vacuum where we have no physical access.

The above challenges were the main driving motivation in developing the Hanle effect field characterization. For simple alignment the process is even easier than the full characterization method detailed previously. One difference to note is that it was not generally helpful to put the beam through a slit when using this procedure. The process is as follows:

1. Block all but a single beam.
2. Place a linear polarizer so the beam is polarized towards a viewport that is perpendicular from the beam direction. There should be two such viewports for each beam.
3. View the fluorescence through the perpendicular port. There should be a dark spot as described in chapter 5.
4. Center the beam on the dark spot in the direction perpendicular to the viewing direction. The beam should now be centered on that axis.
5. Repeat from step 2 with the viewport in the second perpendicular direction.
6. Repeat from step 1 with each beam.

After following the steps above each beam should be aligned so it is passing directly through, and centered on the field zero-point.

Appendix C

Python code

This appendix contains the key components of the python code used for the fitting routines. This code is not complete by itself. Preliminary code loads the image, then stores a subimage centered on the dark-spot in the variable *NumPy* array simageB.

The following codes sets up the model functions to be fit:

```
#select out just the blue bayer pixels
simageB = simage[np.array(simage).mean(2).mean(1).argmax()].copy()
simageB /= simageB.max() # normalize
shp = simageB.shape
simageBW, simageBH = shp[1], shp[0]

# x axis data
xdata = np.array(range(0,simageBW))*pixel*2 # (number pixels)*pixel =
    position in cm (factor of 2 because of bayer pattern)
ydata = np.array(range(0,simageBH))*pixel*2 # (number pixels)*pixel
xcent = (xdata.max()-xdata.min())/2
ycent = (ydata.max()-ydata.min())/2
X, Y = np.meshgrid(xdata, ydata)
dX = np.abs(X[1,1]-X[1,2])
dY = np.abs(Y[1,1]-Y[2,1])

################################################
# Constants
#
# Interpret
```

```
m0 = 9.10938291e-31 # kg                     # electron mass
muB = 9.27401e-24 #A m^2                     # bohr magneton
hbar = 1.054572e-34 #J s                     # reduced plancks
   constant
#gamma = 1.0/2.0*32.0e6  #?                  # inverse damping rate
   of electron oscillations
G = 201e6 # Hz                               # linewidth of
   transition in radians/s
gamma = G/2                                  # decay constant of the
   excited state
L = 10*2.54e-2 # m                           # distance of the
   observer from the zeropoint

#############################################macaulay2
# Model
# convert to 1D tuple problem method
#
def dataUnwrap(data2d) :
    data1d = data2d.copy()
    data1d[1::2,:]=data1d[1::2,::-1]
    return data1d.flatten()

def dataRewrap(data1d,shape) :
    data2d=data1d.reshape(shape)
    data2d[1::2,:]=data2d[1::2,::-1]
    return data2d.copy()

#Approx
def model2D_(x,y, params) :
    A,w,yL,x0,y0,gx,gy = params
    return A*np.exp(-(y-yL)**2/w**2)*(1-1/(1+gx**2*(x-x0)**2+gy**2*(y
       -y0)**2))

#Full
def model2D(x,y, params) :
    A,w,yL,x0,y0,gx,gy = params
    Bx = 2*hbar*gamma/muB*gx*100 # T/cm (converted 1/cm->1/m)
    By = 2*hbar*gamma/muB*gy*100
    xc = (x-x0)/100 # convert to meters and center
    yc = (y-y0)/100 # convert to meters and center
    B = sqrt(Bx**2*xc**2+By**2*yc**2)
    #Coordinates of observer in atom frame:
    Ox = L
    Oy = (By-Bx)/B*xc*yc
```

```
    Oz = (Bx*xc**2-By*yc**2)/B
    Or = np.sqrt(L**2+xc**2+yc**2)
    th = np.arccos(Oz/Or)
    phi = np.arctan(Oy/Ox)
    wLg2 = (gx*(x-x0))**2+(gy*(y-y0))**2
    return A*np.exp(-(y-yL)**2/w**2)*(cos(2*th)+3-2*sin(th)**2*(cos
       (2*phi)+sqrt(wLg2)*sin(2*phi))/(1+wLg2))

#       Numerical interpolation - the intensity vs field data first
   needs to be generated and saved for each saturation value
        fileList = "bruteIntensityDataS.1sqrt.npy","
           bruteIntensityDataS.5sqrt.npy","bruteIntensityDataS10sqrt.
           npy","bruteIntensityDataS100sqrt.npy"
zData = [1,2,3,4]
s0 = np.array([.01,.1,1,10])
i=0;
for f in fileList :
    B_It_data = np.load(f)
    xIntpData = B_It_data[0,:]
    zIntpData = B_It_data[1,:]/B_It_data[1,:].max() # 1 for brute
       data, 2 for apprx data
    zData[i] = zIntpData
    i+=1;
zData = np.array(zData)
spline = scipy.interpolate.RectBivariateSpline(s0,xIntpData,zData,kx
   =1,ky=2 )
I_Intrp2d = lambda x,y:spline.ev(x,y)
s0=1 # This is the peak saturation value at the center of the beam
def model2D(x,y, params) :
    A,w,yL,x0,y0,gx,gy = params
    Bx = hbar*gamma/muB*gx*100 # T/cm (converted 1/cm->1/m)
    By = hbar*gamma/muB*gy*100
    xc = (x-x0)/100 # convert to meters and center
    yc = (y-y0)/100 # convert to meters and center
    B = sqrt(Bx**2*xc**2+By**2*yc**2)
    #Coordinates of observer in atom frame:
    wLg2 = (gx*(x-x0))**2+(gy*(y-y0))**2
    I0 = A*np.exp(-(y-yL)**2/w**2) #-.1*x
    return I0*I_Intrp2d(s0*I0/A,B)*smaskB

# Convert parametic parameter t to x and y values
def model1dUnwrap(t,A,w,yL,x0,y0,gx,gy ) :
    params = [A,w,yL,x0,y0,gx,gy]
    shape = simageB.shape
```

```
    t = t.reshape(shape)
    x = np.array((np.mod(t,shape[1]))*dX)
    y = np.array((np.floor(t/shape[1]))*dY)
    return dataUnwrap(model2D(x,y,params).copy())

###############################################
# initial guesses
# initial parameter guess for intensity
iP1 = np.array([1,.3,ycent,xcent,ycent,3,-6])
```

Then the data is fit, and the gradients are extracted with the following code:

```
####################################################################
# Model Fitting
# Find the optimal fitting parameters and extract the field gradients

# Setup parametric variable T (x-axis for the 1D curve fit)
T = np.arange(simageB.size)

# Find fit
t = cputime() # keep track of how long fitting takes
optimalparams, covmatrix = scipy.optimize.curve_fit(model1dUnwrap, T,
    dataUnwrap(simageB), p0=iP1, maxfev=3000, xtol=1e-8, ftol=1e-8)
print("Time to find fit = {:5.2f}s".format(cputime(t)))

# Interpret parameters
gx = optimalparams[5]
gy = optimalparams[6]
Bx = 2*hbar*gamma/muB*gx*100 # T/m (converted 1/cm->1/m)
By = 2*hbar*gamma/muB*gy*100
print("X gradient fit is {:5.2f} gauss/cm".format(Bx*100))
print("Y gradient fit is {:5.2f} gauss/cm".format(By*100))

# plot model with guess parameters, fit parameters, and the actual
   data
fit = model2D(X,Y,iP1)
fit2 = model2D(X,Y,optimalparams)
fit.min()
fit.max()
simageB.max()
# Plot data and fit model
bounds = [xdata.min(),xdata.max(), ydata.min(), ydata.max()]
fig, ax = plt.subplots(3,1,figsize=(4,8))
_ = ax[0].imshow(fit, cmap='gray', extent = bounds, origin='lower')
_ = ax[0].set_ylabel("Guess")
```

```
_ = ax[1].imshow(fit2, cmap='gray', extent = bounds, origin='lower')
_ = ax[1].set_ylabel("Fit")
_ = ax[2].imshow(simageB, cmap='gray', extent = bounds, origin='lower
    ')
_ = ax[2].set_ylabel("data")
plt.show()
```

Bibliography

[1] C. Roux, A. Emmert, A. Lupascu, T. Nirrengarten, G. Nogues, M. Brune, J.-M. Raimond, and S. Haroche, “Bose-Einstein condensation on a superconducting atom chip,” EPL (Europhysics Letters) **81,** 56004 (2008).

[2] R. Presura, “Hanle effect as candidate for measuring magnetic fields in laboratory plasmas,” Review of Scientific Instruments **83,** 10D528 (2012).

[3] R. Kaiser, N. Vansteenkiste, A. Aspect, E. Arimondo, and C. Cohen-Tannoudji, “Mechanical Hanle effect,” Zeitschrift für Physik D Atoms, Molecules and Clusters **18,** 17–24 (1991).

[4] P. Courteille, S. Muniz, K. Magalhães, R. Kaiser, L. Marcassa, and V. Bagnato, “Magnetic field tomography,” The European Physical Journal D - Atomic, Molecular, Optical and Plasma Physics **15,** 173–180 (2001).

[5] C. V. Nielsen, J. K. Lyngsø, A. Thorseth, M. Galouzis, K. T. Therkildsen, E. D. van Ooijen, and J. W. Thomsen, “Characterization of a magnetic trap by polarization dependent Zeeman spectroscopy,” The European Physical Journal D **48,** 111–119 (2008).

[6] W. Hanle, “Über magnetische Beeinflussung der Polarisation der Resonanzfluoreszenz,” Zeitschrift für Physik **30,** 93–105 (1924).

[7] J. Stenflo, "The Hanle effect and the diagnostics of turbulent magnetic fields in the solar atmosphere," Solar Physics **80,** 209–226 (1982).

[8] C. J. Erickson, "Development of a Strontium-87 Ion Interferometer," Ph.D. thesis, Brigham Young University, 2011.

[9] C. Cohen-Tannoudji, J. Dupont-Roc, G. Grynberg, and P. Thickstun, *Atom-photon interactions: basic processes and applications* (Wiley Online Library, 1992).

[10] G. Moruzzi and F. Strumia, *The Hanle effect and level-crossing spectroscopy* (Springer Science & Business Media, 2013).

[11] R. C. Hilborn, "Einstein coefficients, cross sections, f values, dipole moments, and all that," arXiv preprint physics/0202029 (2002).

[12] W. Hanle, "Über den Zeemaneffekt bei der Resonanzfluoreszenz," Naturwissenschaften **11,** 690–691 (1923).

[13] A. Gallagher and A. Lurio, "Optical Detection of Level Crossing in a J= 1 2 State," Physical Review Letters **10,** 25 (1963).

[14] G. Langer, A. Hochreiner, P. Burgholzer, and T. Berer, "A webcam in Bayer-mode as a light beam profiler for the near infra-red," Optics and Lasers in Engineering **51,** 571 – 575 (2013).

[15] L. M. Richards, S. M. S. Kazmi, J. L. Davis, K. E. Olin, and A. K. Dunn, "Low-cost laser speckle contrast imaging of blood flow using a webcam," Biomed. Opt. Express **4,** 2269–2283 (2013).

[16] "Logitech Forums,", http://forums.logitech.com/t5/Webcams/Interpreting-raw-bayer-data-from-Logitech-cameras/td-p/1391751, 2015, [Online; accessed 24-December-2015].

[17] L. Q. Video Engineering Team, “How to Enable Raw Streaming on Logitech Webcams,”, http://wayback.archive.org/web/20111012174407/http://www.quickcamteam.net/documentation/how-to/how-to-enable-raw-streaming-on-logitech-webcams , 2011, [Online; accessed 24-December-2015].

[18] S. v. d. Walt, S. C. Colbert, and G. Varoquaux, “The NumPy Array: A Structure for Efficient Numerical Computation,” Computing in Science & Engineering **13,** 22–30 (2011).

[19] E. Jones *et al.*, “SciPy: Open source scientific tools for Python,”, http://www.scipy.org/, 2001, [Online; accessed 24-December-2015].